

# An investigation on the thermal performance of volumetric solar absorbers with lateral wall power losses

Jorge E.P. Navalho<sup>a,b,c,\*</sup>, Laura G.G. Silva<sup>d</sup>, José C.F. Pereira<sup>c</sup>

<sup>a</sup> UNIDEMI, Department of Mechanical and Industrial Engineering, NOVA School of Science and Technology, Universidade NOVA de Lisboa, 2829-516, Caparica, Portugal

<sup>b</sup> Laboratório Associado de Sistemas Inteligentes (LASI), 4800-058, Guimarães, Portugal

<sup>c</sup> LAETA, IDMEC, Instituto Superior Técnico, Universidade de Lisboa, Av. Rovisco Pais, 1, 1049-001 Lisboa, Portugal

<sup>d</sup> Departamento de Engenharia Mecânica e Industrial, Faculdade de Ciências e Tecnologia, Universidade Nova de Lisboa, 2829-516 Caparica, Portugal

## ARTICLE INFO

### Keywords:

Concentrated solar energy  
Volumetric solar receiver  
Open-cell foam  
Heat losses  
Insulation  
Numerical simulation

## ABSTRACT

This study investigates the impact of lateral wall heat losses on the performance of volumetric solar absorbers. The effect of absorber dimensions, absorber geometrical parameters and thermophysical properties, and receiver operating conditions on the promotion of lateral heat losses is analyzed. Additionally, the effect of external heat transfer conditions at the absorber lateral wall for a non-insulated receiver is studied. Finally, the combined effects of insulation material and thickness and external heat transfer conditions on the receiver thermal performance are thoroughly investigated. The results show that heat conduction from the absorber solid phase to the absorber lateral wall is the most relevant heat transfer route from the absorber internal region to the lateral wall. A considerable decrease in the receiver thermal efficiency is observed if no insulation were applied — the minimum efficiency decrease in relation to the adiabatic efficiency is about 5.6 percentage points (predicted under natural convection and with black walls). Inappropriate insulation materials may inadvertently promote lateral wall heat losses. An applied insulation layer can effectively transport heat from downstream to upstream absorber regions, potentially aiding in the uniformization of the solid-phase absorber temperature field. The one-dimensional approximation for heat diffusion in the insulation layer yields reasonable results.

## 1. Introduction

Concentrated solar energy can be harvested to produce thermal energy for mechanical and electrical power generation, industrial process heat (heat required for energy-intensive industrial processes), and for driving highly endothermic chemical reactions to produce solar fuels [1–4]. Optical concentrating devices (mirror or reflector surfaces) are required to focus a high amount of solar radiation on a particular surface (absorber) in order to make available such highly concentrated thermal power for a heat transfer fluid circulating in close-contact with the absorber surface. Volumetric solar (directly irradiated) absorbers are a particular type of solar absorbers that allow the penetration of point-focused concentrated solar radiation into the corresponding porous structure volume. The cold heat transfer fluid that is provided to the solar (porous) receiver, withdraws by convective heat transfer a particular fraction of the absorbed concentrated solar irradiation increasing its temperature as it flows from the inlet to the outlet sections. (In volumetric solar absorbers, the surface onto which solar

energy is absorbed is the same from which thermal energy is extracted to the heat transfer fluid.) Porous materials, particularly open-cell foam and honeycomb monolith structures — that are used in a wide variety of applications such as for hydrogen production [5–7] and exhaust gas pollution control [8] — have been highly applied as volumetric solar absorber materials [9–11]. In addition, wire meshes, packed beds, and corrugated metal foils have also been applied as volumetric solar absorbers [12–15]. Alternative (innovative) volumetric absorber designs have also been proposed — see elsewhere [16–18].

The initial development of volumetric solar absorbers (dated back to late 1970's – mid 1980's) was strongly based on experimental (trial-and-error) testing procedures, hand calculations, and proprietary and problem-specific codes [9,19,20]. For approximately the last 15 years, the computing power increase and the availability of sophisticated, highly-reliable, user-friendly, and general-purpose numerical simulation software have contributed to the progress of volumetric solar absorbing technology [9,21]. (This evidence is in full agreement with

\* Corresponding author at: UNIDEMI, Department of Mechanical and Industrial Engineering, NOVA School of Science and Technology, Universidade NOVA de Lisboa, 2829-516, Caparica, Portugal.

E-mail address: [jorge.navalho@fct.unl.pt](mailto:jorge.navalho@fct.unl.pt) (J.E.P. Navalho).

<https://doi.org/10.1016/j.solener.2024.112937>

Received 14 June 2024; Received in revised form 15 August 2024; Accepted 11 September 2024

Available online 3 October 2024

0038-092X/© 2024 The Authors. Published by Elsevier Ltd on behalf of International Solar Energy Society. This is an open access article under the CC BY license (<http://creativecommons.org/licenses/by/4.0/>).

**Nomenclature**

$A$	Area, $m^2$ ; parameter A of Eq. (12), $W m^{-2}$
$B$	Parameter B of Eq. (12), $m^{-2}$
$c_p$	Specific heat, $J kg^{-1} K^{-1}$
$d_c$	Foam mean cell diameter, m
$d_p$	Foam mean pore diameter, m
$G_c$	Collimated (incident) solar irradiation, $W m^{-2}$
$G_d$	Diffusive irradiation, $W m^{-2}$
$H_c$	Collimated (incident) solar irradiation on a wall, $W m^{-2}$
$h$	Specific enthalpy, $J kg^{-1}$ ; convection heat transfer coefficient, $W m^{-2} K^{-1}$
$h_{rad}$	Radiative heat transfer coefficient, $W m^{-2} K^{-1}$
$h_v$	Volumetric convection heat transf. coef., $W m^{-3} K^{-1}$
$\vec{i}_i$	Unit vector in the direction of coordinate $x_i$ , –
$L_{abs}$	Absorber length, m
$\dot{m}$	Mass flow rate, $kg s^{-1}$
$\vec{n}$	Unit outward normal vector, –
$P_{loss}$	Power loss, W
$p_{latWall}^{regain}$	Power regain through the insulation layer, W
$p$	Pressure, Pa
$Q_0$	Total concentrated solar power provided to the receiver, W
$q_0''$	Concentrated solar heat flux at the receiver front section, $W m^{-2}$
$\vec{q}_{rad}$	Radiative heat flux vector, $W m^{-2}$
$R$	Ideal gas constant, $J kmol^{-1} K^{-1}$
$R_{abs}$	Absorber radius, m
$Re$	Local Reynolds number, –
$r$	Transversal (radial) coordinate, m
$T$	Temperature, K
$T_\infty$	Surrounding surfaces and adjoining fluid temperature, K
$t$	Time, s
$U$	Overall heat transfer coefficient, $W m^{-2} K^{-1}$
$u$	Axial component of superficial velocity vector, $m s^{-1}$
$u_i$	Superficial velocity component in the direction of coordinate $x_i$ , $m s^{-1}$
$\vec{u}$	Superficial velocity vector, $m s^{-1}$
$v$	Radial component of superficial velocity vector, $m s^{-1}$
$W$	Molar weight, $kg kmol^{-1}$
$x$	Longitudinal (axial) coordinate, m
<b>Greek symbols</b>	
$\beta$	Extinction coefficient, $m^{-1}$

$\delta_{ins}$	Insulation layer thickness, m
$\epsilon$	Foam strut surface emissivity, –
$\epsilon_w$	Lateral wall surface emissivity, –
$\eta_{th}$	Thermal efficiency, –
$\kappa$	Absorption coefficient, $m^{-1}$
$\lambda$	Thermal conductivity, $W m^{-1} K^{-1}$
$\mu$	Dynamic viscosity, Pa s
$\rho$	Density, $kg m^{-3}$
$\sigma$	Stefan–Boltzmann constant, $W m^{-2} K^{-4}$
$\sigma_s$	Scattering coefficient, $m^{-1}$
$\phi$	Foam porosity, –

**Subscripts and Superscripts**

1D	One-dimensional (insulation model)
A	Adiabatic absorber lateral wall
avg	Average
eff	Effective
ext	External surface; external environment
g	Gas
in	Inlet section
ins	Insulation
int	Internal surface
latWall	Lateral wall
MD	Multi-dimensional (insulation model)
NA	Non-adiabatic absorber lateral wall
out	Outlet section
rad	Radiation
s	Solid
tot	Total
trans	Transmission
w	Wall

trade-off between accuracy and computational cost. According to this approach, no distinction is considered between the actual space occupied by fluid (gas) and solid phases at each local absorber position — therefore, this modeling strategy does not require the definition of the actual complex geometry of the porous structure but mean (global) geometrical parameters. For the calculation of local absorber temperatures, the absorber gas and solid phases may be considered at the same temperature (local thermal equilibrium [LTE] approach) [23–25] or at different temperatures (local thermal non-equilibrium [LTNE] approach) [26–28]. The later approach — that requires the solution of two coupled energy balance equations and suitable correlations to compute convection (interphase) heat transfer rates — is largely preferred in the literature because it provides more reliable results at the expense of a minor increase in the computational cost [22]. Radiative heat transfer (including solar radiation transport) in the receiver porous volume — that plays a fundamental role in the receiver performance — has been generally accounted for through different strategies: (i) the P1 approximation (for absorption, emission, and scattering of radiation other than solar radiation [long-wave radiation]) and the Monte Carlo ray tracing method [29,30] or the Beer's law [31] (for solar radiation [short-wave radiation] transport); (ii) Rosseland (diffusion) approximation or discrete ordinates (long-wave radiation) and Beer's law (short-wave radiation) [32–34]; or, alternatively, (iii) including, simultaneously, long- and short-wave radiation contributions through the modified P1 approximation (considering collimated incident solar radiation) [26,35,36], discrete ordinates method [32], two-flux approximation [27,37] or Monte Carlo method [27]. The solar radiation contribution has also been included in the absorber hydrothermal model formulation according to the so-called surface

the fact that the majority of works found in the literature on this topic is heavily [or exclusively] based on theoretical [numerical] research.)

Different mathematical models have been adopted to predict the hydrothermal performance of volumetric solar receivers (and thermochemical reactors) [9,22]. The volume-averaging (or continuum) approach has been largely preferred mainly due to its well-known

approach, through a second-type [Neumann] boundary condition for the (solid-phase) energy balance equation [36,38] despite the fact that it leads to exaggerated receiver front surface temperatures, particularly for very high porosities and mean pore sizes [29]. Several works have neglected long-wave radiative heat transfer within the absorber volume [39–41] even though this heat transfer mechanism is very relevant at high temperatures.

Several works have compared the results predicted by different model formulations. In particular, comparisons of numerical predictions have been performed in the literature considering: (i) LTE vs. LTNE modeling approaches [42,43]; (ii) different correlations to compute convection heat transfer coefficients [42–46], pressure drop (viscous and inertial momentum losses) [42], and effective and intrinsic thermophysical properties [27,38,46]; (iii) different radiative heat transfer models [27,47,48] and the effect of radiative heat transfer within the absorber volume [42]; (iv) different methods to apply the concentrated solar heat flux distribution (volumetric [collimated and non-collimated] and surface approach) [29,49]; (v) different physical model dimensions (one- vs. multi-dimensional models) [43]; (vi) different boundary conditions [30,36,50] including to evaluate the role of radiative heat loss from the front (irradiated) solid absorber section [36]; and (vii) different computational domains (including or excluding an fluid entry length upstream the absorber region) [43].

In alternative to the volume-averaging approach, pore-scale (direct) numerical simulations can significantly improve the accuracy of results at the cost of remarkably higher computing power. This modeling strategy eliminates the need for externally derived correlations and effective properties to evaluate transport rates. However, this modeling technique requires the geometrical description (representation) of the intricate three-dimensional foam pore network. Fluid flow and energy governing equations are applied to the actual physical space occupied by the fluid phase while the heat diffusion equation are applied to the solid region with consistent conjugate heat transfer conditions between both phases. Since this modeling approach is more elaborated and requires high computational power, only a few works have applied this modeling strategy to the current subject — see elsewhere for simplified (idealized) open-cell foam geometrical models [51,52] and for realistic open-cell foam absorber structures comprising a particular volume of an absorber unit [53–55] and comprising a complete concentrating solar facility (complete solar receiver unit [absorber and absorber enclosure], parabolic dish concentrator [solar collector system], and solar insolation field characteristics) [11]. Currently, this class of models are not suitable for extensive parametric investigations — typically addressed at early design studies — but it can offer valuable insights into unresolved issues and contradictory findings reported in the literature. (More reliable information on the performance of volumetric solar absorbers can be obtained applying pore-scale models rather than experimental investigations, as experimental [intrusive] measurements can affect and perturb the actual receiver performance.) In addition — and as an alternative to exhaustive experimental campaigns —, this class of models has also been widely applied to develop transport correlations and effective properties that are required for volume-averaged models — see elsewhere works directly related to this research field [53,56,57].

Numerical works have been highly concentrated on the effect of geometrical properties (pore size and porosity) of uniform open-cell foam absorber porous structures on the corresponding radiative, hydrodynamic, and thermal performance [26,39,58]. Non-uniform absorber porous (multi-layer open-cell foam or graded) structures along the radial and longitudinal receiver directions have also been highly investigated, particularly, regarding the effect of pore size and porosity distributions [32,34,59,60]. The relevance of thermophysical properties on the receiver solar radiation transport and hydrothermal performance has also been investigated, in particular, the effect of the heat transfer fluid [41,54], the effect of the actual absorber material thermal conductivity [26,61,62], and foam strut (solid ligament) surface emissivity

under spectral non-selective [52,61,63] and selective conditions [37, 52]. The impact of working conditions has also been extensively investigated, namely the role of the inlet fluid velocity [26,39,47,52,58, 62], inlet temperature [33], and concentrated solar heat flux distribution (concentrated solar irradiation distribution at the receiver front section) [25,39,47,62,64,65]. The large majority of numerical works have investigated the operation of porous foam solar absorbers under steady-state conditions but transient studies can also be found [62,65–67].

Large temperature gradients (and very high local temperatures [hot-spots]) in the absorber solid-phase porous structure can be established during steady-state operation primarily due to highly non-uniform concentrated solar flux distributions at the receiver front (irradiated) section [68,69]. Large solid-phase temperature gradients (local overheating) promote high material stress levels which may lead to the receiver structural failure (receiver destruction) [69]. Different works have investigated strategies to improve solid-phase temperature uniformity at the receiver front section and the receiver thermal performance. Chen et al. [28] investigated the potential to reduce solid temperature gradients along the radial direction at the absorber front section through the application of a composite absorber porous structure — absorber composed by a porous foam in the inlet near-wall region with different structural parameters (porosity and mean cell size) than those of the foam at the core of the absorber. They reported a decrease in the solid-phase temperature gradient along the radial direction at the absorber front section and an increase in the mean outlet fluid temperature utilizing the composite absorber structure in comparison with a uniform absorber structure. Du et al. [60] investigated radial-graded volumetric solar receivers through both experimental and numerical methods to address non-uniform solar flux distributions. They found that the efficiency (and the outlet fluid temperature) can be increased considering two cylindrical porous layers along the radial direction with the inner layer having a lower pore density (higher pore diameter) than the outer layer in comparison with the performance evaluated with uniform porous structures. In addition, the authors performed an optimization study considering five cylindrical porous layers along the radial direction and determined the optimal pore diameter for each layer to maximize the thermal efficiency. Nimvari et al. [70] investigated the effect of the inlet fluid velocity radial profile on the solid temperature distribution — the authors propose the operation of volumetric solar absorbers with higher inlet velocities at the central region than at the annular (outer) region to compensate the higher concentrated solar flux values at the central region in relation to the outer region. Similar findings were reported by Shi et al. [71] while improving the matching between the concentrated solar heat flux Gaussian profile and a Gaussian-like inlet fluid velocity profile. For closed-loop (windowed) volumetric solar receivers, Li et al. [72] suggest the application of an annular inner window to reshape the flow field in such a way that higher fluid velocities are attained at locations where high concentrated solar irradiation values are observed (central region).

The porous medium absorber structures of volumetric solar receivers and porous solar thermochemical reactors (volumetric solar receptors) typically have a cylindrical shape with the heat transfer fluid flow (or reacting flow) main direction aligned with the cylindrical porous structure axis. Heat losses through the lateral walls of solar absorber porous media have been generally neglected in the literature. This is observed because the main research focus on this field has been related to absorber internal design considerations and operation conditions — e.g. effect of porous medium type, effect of receiver/reactor geometry and dimensions, effect of porous media geometrical and thermophysical parameters, effect of the inlet fluid velocity, effect of operating pressure, etc. Additionally, neglecting lateral wall heat losses is a convenient approach for model simplification in numerical works. Exceptions are found in works related with the overall receiver/reactor design and ensuing performance characterization and works combining

experimental measurements with numerical predictions — proper consideration of the receptor insulation is required to enhance the accuracy of numerical results. Zhang et al. [73] studied the relevance of foam geometrical parameters (pore size and porosity) on the thermochemical performance of solar-driven methane dry reforming. They considered in the model formulation power losses from the lateral wall of the reactor but its relevance — particularly against the adiabatic lateral wall condition — has not been investigated neither the role of external heat transfer conditions and insulation layer parameters. Moreover, the authors simplified the heat conduction through the lateral (tubular) insulation layer which could affect the results accuracy. Lougou et al. [74] concluded that the insulation thermal conductivity and insulation thickness have a relevant role on the thermal efficiency of thermochemical reactors for the  $\text{CO}_2$ -splitting process considering constant external heat transfer conditions. Similar conclusions were drawn by Dessie et al. [75] which considered different insulating materials and thickness values on the performance of a solar reactor. Ma et al. [76] analyzed the dynamic performance of a  $\text{CO}_2$ -splitting solar thermochemical reactor (during the reduction step) and reported non-negligible heat losses by convection from the outer surface of the reactor insulation domain. Other works — particularly related with solar thermochemical reactors — that take into account heat losses through a thermal insulating lateral region to the surrounding environment can be found in the literature [77,78]. (The literature works presented before considering heat losses through an insulation layer consider the local thermal equilibrium approach).

The vast majority of numerical works available in the literature on common porous media applications in concentrated solar energy (as volumetric solar receivers or solar thermochemical reactors) consider an adiabatic absorber lateral wall — *i.e.*, any heat loss mechanism is neglected at the absorber/receiver lateral wall. Therefore, the deviation between numerical predictions for the receiver performance in relation to the total solar energy conversion condition is only due to energy losses from the front and rear sections — generally by reflection, back-scattering, re-emission, and transmission and for windowed volumetric solar receiver by convection from the window. As far as the authors are aware, no detailed, thorough, and rigorous investigation has been carried out on the relevance of power losses through the volumetric solar receiver lateral wall considering multi-dimensional heat conduction models for the insulation layer and different surface heat loss mechanisms and external conditions. Comparison between the thermal performance of receivers with adiabatic and non-adiabatic absorber lateral walls is incomplete. This work intends to fill this gap.

In this work, the impact of absorber lateral wall heat losses on the performance of volumetric solar receivers is comprehensively investigated at different levels. Firstly, the effect of the absorber dimensions, absorber (porous foam) geometrical parameters and thermophysical properties, and receiver operating conditions on lateral wall heat losses is investigated. To conduct this study, two extreme heat transfer conditions are considered at the absorber lateral wall: (i) adiabatic condition; and (ii) constant temperature (equal to the external environment temperature) condition — maximum lateral wall power loss condition. Subsequently, the effect of external heat transfer conditions — that govern convection and radiation thermal energy losses from the absorber lateral wall — is investigated neglecting the application of any insulation layer onto the absorber lateral wall. Finally, the combined effects of insulation material, insulation thickness, and external heat transfer conditions on the receiver thermal performance are thoroughly investigated according to the results of a multi-dimensional heat conduction model for the insulation layer. In addition, this work also analyzes the prediction performance and suitability of the one-dimensional heat diffusion approach for the insulation layer — this model is more competitive and advantageous in terms of computational cost than multi-dimensional models.

The structure of this paper is as follows. In Section 2, the physical model of the volumetric solar receiver considered in this work is

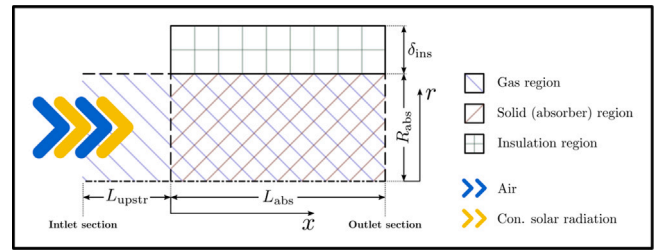


Fig. 1. Two-dimensional (axisymmetric) schematic representation of the volumetric solar receiver.

introduced. In Section 3, mathematical and numerical model details are presented, and model validation — taking into account reference data available in the literature — is provided. Section 4 covers the results and discussion. Finally, this paper concludes with concise findings outlined in Section 5.

## 2. Physical model

Fig. 1 presents the physical model of the volumetric solar receiver under consideration. The receiver comprises a cylindrical-shaped absorber for solar radiation and a thermal insulation material applied to its lateral surface. The absorber is composed of a porous foam structure with a forced air flow directed along its axis. The absorber radius and length are referred to as  $R_{\text{abs}}$  and  $L_{\text{abs}}$ , respectively. In Fig. 1, Section  $x = 0$  corresponds simultaneously to the absorber fresh air inlet section and to the absorber solar irradiated (front) section. The front section center point of the volumetric solar absorber (origin of the coordinate system in Fig. 1) is placed at the focal point of a parabolic dish concentrating system. To improve the accuracy of numerical predictions, the gas region is extended upstream the absorber front section along 0.03 m ( $L_{\text{upstr}}$ ) — *i.e.*, the fluid region entrance section is positioned at  $x = -L_{\text{upstr}}$ . The receiver outlet section (absorber rear section) is located at  $x = L_{\text{abs}}$ . (Previous investigations revealed that extending the fluid domain downstream the porous structure exit section does not lead to significant accuracy benefits [43].) The insulation layer has a thickness of  $\delta_{\text{ins}}$  — the insulation region extends from  $r = R_{\text{abs}}$  to  $r = R_{\text{abs}} + \delta_{\text{ins}}$  and has a length equal to  $L_{\text{abs}}$  — see Fig. 1. Radiation and convection power losses from the receiver lateral wall are accounted for at the outer surface of the insulation layer ( $r = R_{\text{abs}} + \delta_{\text{ins}}$ ).

## 3. Mathematical and numerical models

The volume-averaging approach is considered for the mathematical model of the absorber fluid and solid phases. Since the receiver has constant geometrical parameters, properties, and conditions along the circumferential (angular) direction, a two-dimensional axisymmetric model is considered. The following assumptions are applied: (i) the receiver operation is stationary (time-independent); (ii) the fluid (air) behaves as an ideal gas; (iii) the fluid flow is laminar and incompressible (weakly compressible); (iv) body forces (*e.g.* gravitational force) play a negligible role on the governing equations; (v) the porous medium geometrical parameters and thermophysical properties are constant and homogeneous; (vi) the solid porous matrix structure is assumed as a gray and an optically dense medium with absorption, emission, and isotropic scattering; (vii) gas (fluid phase) is radiatively non-participating (transparent to radiation); (viii) thermal contact resistance between the absorber domain and the insulation region is negligible; and (ix) the internal surface of the absorber lateral wall and external surface of the insulation layer are opaque, gray, and diffusive.

### 3.1. Governing equations

#### 3.1.1. Continuity and momentum balance equations

Fluid flow is governed by the mass conservation (continuity) equation and momentum balance equations that are given by Eqs. (1) and (2), respectively. In Eqs. (1)–(2),  $\vec{u}$ ,  $p$ ,  $\mu_g$ ,  $\rho_g$ , and  $\phi$  represent the superficial velocity vector, pressure, dynamic viscosity, density, and porosity, respectively. (Air density and dynamic viscosity are temperature-dependent thermophysical properties, and consequently, the velocity and pressure field distributions are dependent on the fluid temperature field distribution [solution of the fluid energy balance equation].)

$$\phi \frac{\partial \rho_g}{\partial t} + \nabla \cdot (\rho_g \vec{u}) = 0 \quad (1)$$

$$\phi \frac{\partial (\rho_g u_i)}{\partial t} + \nabla \cdot (\rho_g u_i \vec{u}) = \nabla \cdot \left\{ \mu_g \nabla u_i + \left[ \mu_g (\nabla \vec{u})^T - p - \frac{2}{3} \mu_g \nabla \cdot \vec{u} \right] \vec{i}_i \right\} + S_{M,i} \quad (2)$$

The momentum balance equation source term ( $S_{M,i}$ ) — which accounts for momentum losses in the porous medium — is computed with Eq. (3), where  $d_c$  is the porous foam mean cell diameter. This correlation was developed based on both experimental and numerical results and is suitable over the ranges for porosity and Reynolds number given by  $0.66 < \phi < 0.93$  and  $10 < Re \equiv \rho_g |\vec{u}| d_c / \mu_g < 400$ , respectively [79]. This correlation has found extensive application in existing literature [30,49,80].

$$S_{M,i} = - \frac{1039 - 1002\phi}{d_c^2} \mu_g u_i - \frac{0.5138\phi^{-5.739}}{d_c} \rho_g |\vec{u}| u_i \quad (3)$$

Eqs. (1)–(2) are applied to the absorber (fluid) region and the absorber upstream (single-phase) region. Upstream the absorber region (where no porous structure is available), the porosity and the momentum balance equation source terms are set to unity and zero, respectively. Despite being applied to incompressible flow and steady-state conditions, the set of governing equations herein presented retains the corresponding terms for thoroughness and generality.

#### 3.1.2. Energy balance equations

The local thermal non-equilibrium approach — that requires separate energy conservation equations for the absorber solid and gas phases — is herein applied to evaluate the receiver temperature distribution as it is commonly recommended in the literature [27,43]. In addition, since the receiver is composed by an insulation layer surrounding the absorber lateral wall, the corresponding temperature distribution is obtained with an independent energy balance equation.

*Gas-phase energy balance equation.* Eq. (4) corresponds to the energy balance equation for the receiver gas phase. The effective gas thermal conductivity is given by Eq. (5) as commonly considered in the literature [26,38,81]. In Eqs. (4)–(5),  $T_g$ ,  $T_s$ ,  $c_{p,g}$ ,  $h_v$ , and  $\lambda_g$  are the gas temperature, solid temperature, gas specific heat, volumetric convection heat transfer coefficient, and clear (intrinsic) fluid thermal conductivity, respectively.

$$\phi \frac{\partial (\rho_g c_{p,g} T_g)}{\partial t} + \nabla \cdot (\rho_g c_{p,g} \vec{u} T_g) = \nabla \cdot (\lambda_{g,\text{eff}} \nabla T_g) + h_v (T_s - T_g) \quad (4)$$

$$\lambda_{g,\text{eff}} = \phi \lambda_g \quad (5)$$

For the porous medium structure and hydrothermal conditions under consideration, the local convection coefficient can be calculated with the correlation obtained by Wu et al. [56] through pore-scale numerical simulations that is given by Eq. (6). This correlation has seen widespread application in the literature [29,38,43,49] and is valid along the ranges  $0.66 < \phi < 0.93$  and  $70 < Re \equiv \rho_g |\vec{u}| d_c / \mu_g < 800$  [56].

$$h_v = \frac{\lambda_g Re^{0.438}}{d_c^2} (32.504\phi^{0.38} - 109.94\phi^{1.38} + 166.65\phi^{2.38} - 86.98\phi^{3.38}) \quad (6)$$

*Solid-phase energy balance equation.* Eq. (7) corresponds to the absorber solid-phase temperature governing equation. The effective solid thermal conductivity is given by Eq. (8) [81,82]. In Eqs. (7)–(8),  $c_{p,s}$  and  $\lambda_s$  correspond to the solid intrinsic (single-phase) specific heat and thermal conductivity, respectively. The source term of Eq. (7) ( $S_{\text{rad}}$ ) takes into account the net radiative power contribution in the absorber structure. This contribution is evaluated through the application of a particular radiative heat transfer model — see Section 3.1.3.

$$(1 - \phi) \frac{\partial (\rho_s c_{p,s} T_s)}{\partial t} = \nabla \cdot (\lambda_{s,\text{eff}} \nabla T_s) - h_v (T_s - T_g) + S_{\text{rad}} \quad (7)$$

$$\lambda_{s,\text{eff}} = \frac{1}{3} (1 - \phi) \lambda_s \quad (8)$$

*Insulation energy balance equation.* Eq. (9) corresponds to the energy balance equation for the insulation region. In Eq. (9),  $\rho_{\text{ins}}$ ,  $c_{p,\text{ins}}$ ,  $T_{\text{ins}}$ , and  $\lambda_{\text{ins}}$  correspond to the insulation density, specific heat, temperature, and thermal conductivity, respectively.

$$\frac{\partial (\rho_{\text{ins}} c_{p,\text{ins}} T_{\text{ins}})}{\partial t} = \nabla \cdot (\lambda_{\text{ins}} \nabla T_{\text{ins}}) \quad (9)$$

#### 3.1.3. Radiative transfer equation

For high-temperature concentrated solar energy applications, the radiative heat transfer equation has been solved through various models in the literature [22,43]. Particularly for volumetric solar absorbers, the modified P1 approximation has been widely considered in the literature [26,27,47,73,83,84]. The modified P1 approximation is given by Eq. (10), where  $\kappa$ ,  $\sigma_s$ ,  $G_d$ , and  $G_c$  correspond to the porous medium absorption coefficient, porous medium scattering coefficient, diffusive irradiation, and collimated solar irradiation, respectively. Eq. (10) is applied to the absorber region.

$$-\nabla \cdot \left( \frac{1}{3(\kappa + \sigma_s)} \nabla G_d \right) = \kappa (4\sigma T_s^4 - G_d) + \sigma_s G_c \quad (10)$$

The solar irradiation local value in the absorber domain is given by Eq. (11). In this equation,  $q_0''$  is the incident concentrated solar radiation flux at Section  $x = 0$  (see Fig. 1), while  $\beta$  denotes the porous medium extinction coefficient.

$$G_c(r, x) = q_0''(r) \exp(-\beta x) \quad (11)$$

The incident concentrated solar radiation flux at the receiver front section is computed with Eq. (12). This equation has been largely applied as a curve fitting for concentrated solar irradiation profiles obtained with parabolic dish assemblies [31,60,85,86]. In Eq. (12), constants (parameters)  $A$  and  $B$  specify the profile maximum value (registered at the receiver centerline) and the profile shape along the radial direction, respectively. (Parameter  $B$  equal to zero corresponds to a uniform profile while increasing this parameter leads to an increasingly non-uniform profile along the radial direction.)

$$q_0''(r) = A \exp(-Br^2) \quad (12)$$

The radiative source term required in Eq. (7) is computed with Eq. (13). Eq. (13) requires the solution for the diffusive irradiation field according to the application of the modified P1 approximation.

$$S_{\text{rad}} \equiv -\nabla \cdot \vec{q}_{\text{rad}} = -\kappa [4\sigma T_s^4 - (G_d + G_c)] \quad (13)$$

### 3.2. Thermodynamic, transport, and radiative properties

The gas density and dynamic viscosity are evaluated through the perfect gas law (Eq. (14)) and Sutherland law (Eq. (15)), respectively. In Eq. (15),  $\mu_0$ ,  $T_0$ , and  $S$  are equal to  $1.71 \times 10^{-5} \text{ Pa s}^{-1}$ , 273 K, and 110.4 K, respectively, in accordance with Ref. [87].

$$\rho_g = \frac{p W_g}{RT_g} \quad (14)$$

$$\frac{\mu_g}{\mu_0} = \left(\frac{T_g}{T_0}\right)^{3/2} \left(\frac{T_0 + S}{T_g + S}\right) \quad (15)$$

The gas specific heat and thermal conductivity are temperature-dependent properties calculated in accordance with Eqs. (16) and (17), respectively. In these equations, the actual gas temperature ( $T_g$ ) is provided in kelvins [11]. The gas specific enthalpy is computed with Eq. (18).

$$c_{p,g} \text{ (J kg}^{-1} \text{ K}^{-1}\text{)} = 1.0703 \times 10^3 - 5.3090 \times 10^{-1} T_g + 1.3251 \times 10^{-3} T_g^2 - 9.6767 \times 10^{-7} T_g^3 + 2.4422 \times 10^{-10} T_g^4 \quad (16)$$

$$\lambda_g \text{ (W m}^{-1} \text{ K}^{-1}\text{)} = -5.2076 \times 10^{-3} + 1.2940 \times 10^{-4} T_g - 9.1803 \times 10^{-8} T_g^2 + 3.4288 \times 10^{-11} T_g^3 \quad (17)$$

$$h_g(T_g) = \int_{T_{ref}}^{T_g} c_{p,g}(T) dT \quad (18)$$

The porous foam absorption, scattering, and extinction coefficients are calculated according to Eqs. (19), (20), and (21), respectively. (In this work, no distinction is made between the mean cell diameter and mean pore diameter, *i.e.*  $d_p = d_c$ , as it is usual in the literature [29,30,88–91].)

$$\kappa = \frac{3\varepsilon(1-\phi)}{2d_p} \quad (19)$$

$$\sigma_s = \frac{3(2-\varepsilon)(1-\phi)}{2d_p} \quad (20)$$

$$\beta \equiv \kappa + \sigma_s = \frac{3(1-\phi)}{d_p} \quad (21)$$

### 3.3. Boundary and interface conditions

At the fluid entrance section ( $x = -L_{upstr}$  — see Fig. 1), the fluid velocity components and temperature are prescribed in accordance with Eqs. (22)–(23) and (24), respectively.

$$u = u_{in} \quad (22)$$

$$v = 0 \quad (23)$$

$$T_g = T_{g,in} \quad (24)$$

At the receiver centerline ( $r = 0$ ), Eqs. (23) and (25)–(28) are applied in order to represent axial symmetry conditions. (In these equations,  $\vec{n}$  represents the unit outward normal vector to the boundaries where the equations are applied.)

$$\nabla u \cdot \vec{n} = 0 \quad (25)$$

$$\nabla T_g \cdot \vec{n} = 0 \quad (26)$$

$$\nabla T_s \cdot \vec{n} = 0 \quad (27)$$

$$\nabla G_d \cdot \vec{n} = 0 \quad (28)$$

At the absorber lateral wall ( $r = R_{abs}$ ), the no-slip (and impermeable [impenetrability]) conditions are imposed (see Eq. (29)) and thermal equilibrium between the absorber solid and gas phases is considered (Eq. (30)).

$$u = v = 0 \quad (29)$$

$$T_g = T_s \quad (30)$$

The Marshak's boundary condition (Eq. (31)) is applied at the boundaries of the domain (other than the symmetry axis) where the governing equation of the diffusive irradiation (modified P1 approximation) is solved — boundaries  $x = 0$ ,  $x = L_{abs}$  and  $r = R_{abs}$ . In Eq. (31),  $T_w$  and

$\varepsilon_w$  correspond to the temperature and surface emissivity, respectively, of the boundary under consideration. Particularly, for the front section ( $x = 0$ ) and rear section ( $x = L_{abs}$ ),  $T_w$  is equal to  $T_{g,in}$  and to the average outlet gas temperature (downstream manifold effective surface temperature), respectively. At the absorber lateral wall ( $r = R_{abs}$ ),  $T_w$  is equal to the local absorber gas (and solid) temperatures. The surface emissivity ( $\varepsilon_w$ ) is assigned a value of 1.0 at the absorber front and rear sections and referred to as  $\varepsilon_{w,int}$  for the internal surface of the absorber lateral wall. At the lateral wall the collimated irradiation ( $H_c$ ) is negligible because the concentrated (collimated) solar radiation provided to the receiver is aligned with the receiver axis.

$$\vec{q}_{rad} \cdot \vec{n} \equiv -\frac{1}{3\beta} \nabla G_d \cdot \vec{n} = -\frac{\varepsilon_w (4\sigma T_w^4 - G_d) + 4(1 - \varepsilon_w) H_c}{2(2 - \varepsilon_w)} \quad (31)$$

At the absorber front section ( $x = 0$ ) and rear section ( $x = L_{abs}$ ), the absorber solid phase is adiabatic — *i.e.*, Eq. (27) applies. At the outer surface of the upstream (single-phase) fluid region ( $x < 0$  and  $r = R_{abs}$ ), Eqs. (23) and (25)–(26) are applied. At the fluid outlet section, negligible axial gradients for solved fluid scalars and zero static gauge pressure are considered.

The remaining boundary condition that must be defined corresponds to the boundary condition for the solid temperature governing equation (solid-phase energy balance equation) at the absorber lateral wall surface ( $r = R_{abs}$  and  $0 < x < L_{abs}$ ). This boundary condition is defined in accordance with the particular model applied to take into account the insulation layer — see Sections 3.3.1–3.3.2.

#### 3.3.1. One-dimensional insulation heat conduction approach

According to the one-dimensional insulation model, the boundary condition for the solid temperature at the absorber lateral wall surface is given by Eq. (32). This equation represents an energy balance to the absorber lateral wall surface taking into account conduction heat transfer from the absorber solid and fluid phases, net radiative heat transfer to the absorber lateral wall surface, and power losses through the insulation layer.

$$\lambda_{s,eff} \nabla T_s \cdot \vec{n} = -\lambda_{g,eff} \nabla T_g \cdot \vec{n} + \vec{q}_{rad} \cdot \vec{n} - U(T_s - T_\infty) \quad (32)$$

The one-dimensional insulation model considers heat diffusion in the insulation layer exclusively along the radial direction. Moreover, under steady-state conditions and no heat generation in the insulation layer, the thermal resistance concept can be readily applied to develop an overall heat transfer coefficient ( $U$ ) between the absorber lateral wall surface and the external environment (fluid and surrounding surfaces) defined in relation to the absorber lateral wall surface — see Eq. (33). According to Eq. (33), convection and radiative heat losses are accounted for at the insulation outer surface ( $r = R_{abs} + \delta_{ins}$ ). At the insulation outer surface, the adjoining fluid and surrounding surfaces are at the same temperature (environment temperature,  $T_\infty$ ).

$$U = \left\{ R_{abs} \left\{ \frac{\ln[(R_{abs} + \delta_{ins})/R_{abs}]}{\lambda_{ins}} + \frac{1}{(R_{abs} + \delta_{ins})(h + h_{rad})} \right\} \right\}^{-1} \quad (33)$$

The radiative heat transfer coefficient — strongly dependent on the surface temperature — is computed with Eq. (34), where  $\varepsilon_{w,ext}$  is the emissivity of the insulation external surface.

$$h_{rad} = \varepsilon_{w,ext} \sigma (T_{ins,ext} + T_\infty) (T_{ins,ext}^2 + T_\infty^2) \quad (34)$$

The external surface temperature of the receiver lateral (insulation) wall ( $T_{ins,ext}$ ) — *i.e.*, the receiver temperature at  $r = R_{abs} + \delta_{ins}$  — required in Eq. (34) is computed in accordance with Eq. (35).

$$\frac{\lambda_{ins} (T_{ins,int} - T_{ins,ext})}{\ln[(R_{abs} + \delta_{ins})/R_{abs}]} = (R_{abs} + \delta_{ins}) \times \left[ \varepsilon_{w,ext} \sigma (T_{ins,ext}^4 - T_\infty^4) + h (T_{ins,ext} - T_\infty) \right] \quad (35)$$

In this equation,  $T_{\text{ins,int}}$  corresponds to the internal surface temperature of the receiver lateral (insulation) wall — that is equal to the absorber solid-phase temperature ( $T_s$ ) at  $r = R_{\text{abs}}$  since a negligible thermal contact resistance is considered. While the lateral wall convection heat transfer coefficient is considered constant, the radiative heat transfer coefficient value varies along the longitudinal coordinate because the lateral wall internal surface temperature ( $T_{\text{ins,int}}$ ) — required to compute  $T_{\text{ins,ext}}$  and then  $h_{\text{rad}}$  (see Eqs. (34)–(35)) — depends on the distance from the absorber front section. For a particular combination of insulation thermal conductivity, insulation thickness, external convection heat transfer coefficient, and lateral wall external surface emissivity, the solution for Eq. (35) was computed for  $T_{\text{s,int}}$  in the range between  $T_\infty$  and the maximum absorber lateral wall temperature computed with no lateral wall power losses, considering a temperature increment equal to 1 K. Afterwards, the radiative heat transfer coefficient was calculated (according to Eq. (34)) and a table storing the correspondence between  $T_{\text{ins,int}}$  and  $h_{\text{rad}}$  was obtained. Linear interpolation was considered to obtain the radiative heat transfer coefficient for any value of  $T_{\text{ins,int}}$  stored in the referred table.

The boundary condition given by Eq. (32) is also applied for the adiabatic absorber lateral wall condition considering a negligible overall heat transfer coefficient.

### 3.3.2. Multi-dimensional insulation heat conduction approach

According to the multi-dimensional insulation model, the boundary condition for the solid temperature at the absorber lateral wall surface is given by Eq. (36). In this equation, the last term on the right-hand side corresponds to the heat conduction flux to the insulation layer. The multi-dimensional insulation model solves the temperature field at the insulation layer in accordance with the heat diffusion equation — see Eq. (9). For the insulation temperature governing equation, Eqs. (37) and (38) are applied at the insulation inner surface and at the insulation outer surface, respectively. The insulation boundaries  $x = 0$  and  $x = L_{\text{abs}}$  are assumed as adiabatic surfaces — Eq. (39) is applied at these boundaries.

$$\lambda_{s,\text{eff}} \nabla T_s \cdot \vec{n} = -\lambda_{g,\text{eff}} \nabla T_g \cdot \vec{n} + \vec{q}_{\text{rad}} \cdot \vec{n} - \lambda_{\text{ins}} \nabla T_{\text{ins}} \cdot \vec{n} \quad (36)$$

$$T_{\text{ins}} = T_s \quad (37)$$

$$\lambda_{\text{ins}} \nabla T_{\text{ins}} \cdot \vec{n} = -h (T_{\text{ins}} - T_\infty) - \varepsilon_{w,\text{ext}} \sigma (T_{\text{ins}}^4 - T_\infty^4) \quad (38)$$

$$\nabla T_{\text{ins}} \cdot \vec{n} = 0 \quad (39)$$

### 3.4. Numerical models

Governing equations provided with boundary and interface conditions and closure models are numerically solved with the software STAR-CCM+ — CFD software developed by Siemens Digital Industries Software. STAR-CCM+ was applied for geometry and grid development. Convective terms of governing equations are discretized in accordance with the second-order upwind differencing scheme. SIMPLE algorithm is considered to take into account the pressure–velocity coupling and the solution of the complete system of discretized model equations. The passive scalar feature available in STAR-CCM+ was exploited to implement the radiation model considered in this work (modified P1 approximation). Overlapping solution domains — with similar spatial discretization (mesh) features — were considered for the absorber fluid-phase transport equations, absorber solid-phase energy balance equation, and diffusive irradiation governing equation. This procedure coupled with data (solution fields) storage in constantly (every iteration) updating tables provides a reliable and accurate access to the solution fields of different sets of governing equations (data mapping). Within the STAR-CCM+ package, field functions were developed to evaluate thermophysical properties, volumetric external (interphase) heat transfer coefficients, source terms for transport equations, and

boundary conditions. To establish a converged solution, the maximum value for residuals was set below  $10^{-6}$  for all solved governing equations. Wolfram Mathematica was applied to evaluate the insulation outer surface temperature according to the one-dimensional insulation model.

### 3.5. Model verification

Verification corresponds to the procedure of establishing that the mathematical model equations are solved accurately — confirming that numerical models implemented in the software are functioning correctly [92]. Model verification is herein assessed comparing the current model results with reference results available in the literature. Two sets of benchmark results related to the performance of a particular volumetric solar receiver are herein considered. The volumetric solar receiver has a length ( $L_{\text{abs}}$ ) equal to 0.05 m and radius ( $R_{\text{abs}}$ ) of 0.03 m. The two sets of results differ only on the operating condition, particularly, on the inlet gas velocity profile ( $u_{\text{in}}(r)$ ) considered: one set of results is related with a constant inlet gas velocity profile (equal to  $0.8 \text{ m s}^{-1}$ ), while the other is related to a non-uniform inlet gas velocity profile (equal to  $2.4 \text{ m s}^{-1}$  for  $0 \leq r < R_{\text{abs}}/3$  and  $0.6 \text{ m s}^{-1}$  otherwise).

For both sets of results, the inlet gas temperature and solar irradiation profile at the receiver front section correspond to  $300 \text{ K}$  and  $1.5 \exp(-2560r^2) \text{ MW m}^{-2}$ , respectively. The absorber (SiC open-cell foam) porosity and cell size are equal to 0.9 and 2.0 mm, respectively. Results gathered from Chen et al. [28] and Nimvari et al. [70] are taken into account for verification purposes — both works provide data for the constant inlet velocity profile condition and only the later for the non-uniform velocity profile condition. (Required thermophysical intrinsic and effective properties and interphase transport correlations are in agreement with those provided in such references.) For the constant inlet velocity profile case, Figs. 2(a) and 2(b) present the corresponding axial solid- and gas-phase temperature profiles at the receiver centerline and solid temperatures along the radial direction at the irradiated section of the receiver, respectively. The results computed in this work are in very good agreement against the benchmark results, particularly against the results reported by Chen et al. Concerning the pressure drop along the absorber structure, this work predicts a value approximately equal to 151.7 Pa while the works conducted by Chen et al. and Nimvari et al. report 151.3 Pa and 147.0 Pa, respectively. For the non-uniform inlet velocity profile, Fig. 3 presents the centerline solid- and gas-phase temperatures along the absorber longitudinal direction computed in this work and reported by Nimvari et al. A fairly good matching between both results is observed. A successful verification of the actual mathematical model implementation is concluded by comparing the obtained results with benchmark results available in the literature.

## 4. Results and discussion

In this work and unless otherwise stated, the receiver operating condition, geometrical parameters, and thermophysical properties take the reference values presented in Table 1. The reference values listed in Table 1 have been widely considered in the literature — see Refs. [28, 30, 63, 70, 85]. (Particularly, the values considered for the intrinsic thermal conductivity and strut surface emissivity are typical values for SiC open-cell foam structures [27, 52, 70, 85].) In addition, the temperature of the lateral wall external environment (adjoining gas and surrounding surfaces,  $T_\infty$ ) is equal to the receiver inlet gas temperature (300 K). For the stated reference values, the total power provided to the receiver ( $Q_0$ ) accounts for about 1656.96 W, while the relative transmission power loss ( $P_{\text{loss}}^{\text{trans}}/Q_0 \equiv \exp(-\beta L_{\text{abs}})$ ) is negligible.

The relevance of lateral wall heat losses on the solar receiver thermal performance will be comprehensively investigated considering the following hierarchical approach. The effect of parameters, properties, and conditions not pertaining to the insulation layer and lateral wall external environment realms — *i.e.*, parameters, properties, and

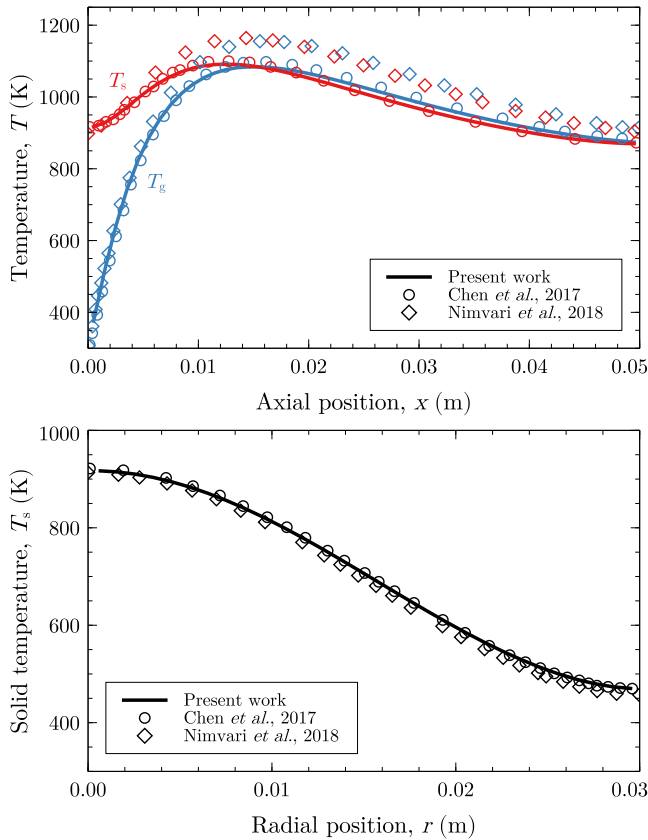


**Fig. 2.** Receiver model verification considering a uniform inlet gas velocity profile: (a) centerline solid and fluid temperature profiles; and (b) solid temperature profiles along the radial direction at the absorber front surface. ((a) and (b): top and bottom, respectively. This labeling scheme will apply throughout this document.) Benchmark results gathered from Chen et al. [28] and Nimvari et al. [70].

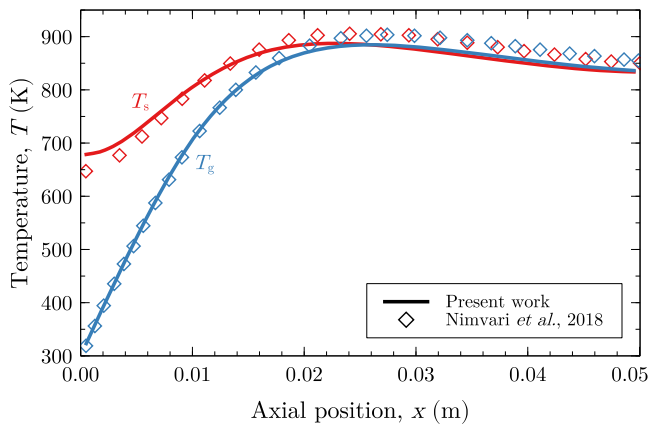


**Fig. 3.** Receiver model verification considering a non-uniform inlet gas velocity profile: centerline solid and fluid temperature profiles. Benchmark results gathered from Nimvari et al. [70].

conditions exclusively related to the inner region of the receiver (absorber region) — is firstly investigated considering two extreme power loss conditions through the absorber lateral wall — see Section 4.1. Afterwards, the effect of lateral wall external heat transfer conditions is investigated neglecting the application of an insulation layer (negligible insulation conduction resistance) — see Section 4.2. Finally, the effect of the insulation layer thickness and insulation thermal conductivity is investigated with a fully distributed (multi-dimensional) heat diffusion

**Table 1**

Reference values for the receiver operating condition, geometrical parameters, and thermophysical properties.

Op. condition / Geo. parameter / Ther. property	Value
Inlet gas velocity, $u_{in}$ (m s <sup>-1</sup> )	1.0
Inlet gas temperature, $T_{g,in}$ (K)	300.0
Parameter $A$ (W m <sup>-2</sup> ) — Eq. (12)	$1.5 \times 10^6$
Parameter $B$ (m <sup>-2</sup> ) — Eq. (12)	2560.0
Absorber length, $L_{abs}$ (m)	0.05
Absorber radius, $R_{abs}$ (m)	0.03
Mean cell diameter, $d_c \times 10^3$ (m)	2.0
Foam porosity, $\phi$ (-)	0.8
Intrinsic solid thermal conductivity, $\lambda_s$ (W m <sup>-1</sup> K <sup>-1</sup> )	80.0
Strut surface emissivity, $\epsilon$ (-)	0.90
Lateral wall internal surface emissivity, $\epsilon_{w,int}$ (-)	0.80

model for the insulation layer, while considering different lateral wall external heat transfer conditions — see Section 4.3. In addition, the prediction suitability (model solution accuracy) of a one-dimensional approach for heat conduction along the radial direction of the insulation layer is assessed by comparing the corresponding results against the multi-dimensional model results — see Section 4.4.

**4.1. Effect of receiver internal parameters, properties, and conditions on lateral wall heat losses**

The effect of absorber dimensions, absorber structure (porous medium) geometrical parameters and thermophysical properties, and receiver operating conditions is herein investigated. In this study, two limit heat transfer conditions at the absorber lateral wall are considered: (i) zero power loss condition through the absorber lateral wall — shortly referred to as the adiabatic absorber lateral wall condition; and (ii) maximum lateral wall power loss condition — shortly referred to as the non-adiabatic absorber lateral wall condition. The later condition is achieved neglecting the overall thermal resistance between the absorber lateral wall ( $r = R_{abs}$ ) and the external environment — *i.e.*, simultaneously neglecting the application of an insulation layer ( $\delta_{ins} = 0$ ) and considering an infinite external overall heat transfer coefficient ( $U_{ext} \equiv h + h_{rad}$ ). (Under such conditions, Eqs. (32)–(33) state that the absorber lateral wall and the external environment are at thermal equilibrium [ $T_s = T_\infty$ ].)

Fig. 4 presents the solid- and gas-phase temperature distributions for the adiabatic and non-adiabatic absorber lateral wall conditions computed considering the reference values stated before. A non-uniform temperature distribution along the radial direction for the adiabatic lateral wall condition is mainly observed due to the non-uniform concentrated solar flux distribution at the absorber front section — the no-slip velocity boundary condition applied at the lateral wall also contributes to non-uniform velocity and thermal profiles but in a significantly lower extent. For the non-adiabatic receiver, heat losses through the lateral wall contribute even more remarkably to increase the temperature variations along the radial direction. These two limits for the receiver operation provide a solar-to-thermal energy conversion efficiency — shortly, thermal efficiency (see Eqs. (40)–(41)) — approximately equal to 83.3% and 19.8% for the adiabatic and non-adiabatic conditions, respectively.

$$\eta_{th} = \frac{\dot{m} (h_{g,out}^{avg} - h_{g,in}^{avg})}{Q_0} \tag{40}$$

$$h_g^{avg} = \frac{\int_A \rho_g h_g u dA}{\dot{m}} \tag{41}$$

For the adiabatic absorber lateral wall, the power loss is mainly due to a net radiative heat transfer from the receiver internal porous structure through the receiver front section toward the external surroundings — radiative heat losses from the absorber through the outlet section

account for less than 1% of the total power loss ( $P_{\text{loss}}^{\text{tot}} \equiv Q_0 (1 - \eta_{\text{th}})$ ). For the non-adiabatic absorber lateral wall, radiative power losses through the inlet section amount to 20.6% of the total power loss while most of the remaining fraction (about 79.2%) is observed through the lateral wall ( $P_{\text{loss}}^{\text{latWall}}$ ) — radiative power losses through the outlet section are negligible (<0.5%). The power loss registered through the lateral wall is computed in accordance with Eq. (42) and has the following three contributions: (i) diffusive heat flux from the absorber gas phase; (ii) diffusive heat flux from absorber solid phase; and (iii) net radiative heat flux from the internal absorber pore structure.

$$P_{\text{loss}}^{\text{latWall}} = - \int_A (\lambda_{s,\text{eff}} \nabla T_s \cdot \vec{n} + \lambda_{g,\text{eff}} \nabla T_g \cdot \vec{n} - \vec{q}_{\text{rad}} \cdot \vec{n}) dA \quad (42)$$

The most relevant contribution to the lateral wall power loss is due to the heat conduction from the solid phase (about 96.8%). Heat conduction from the gas phase is the most negligible contribution on the total lateral wall power loss — it accounts for about 0.3%. Solid-phase heat conduction has a higher contribution than gas-phase conduction in accordance with the higher effective solid thermal conductivity (about  $5.333 \text{ W m}^{-1} \text{ K}^{-1}$ ) than the effective gas thermal conductivity (about  $0.021 \text{ W m}^{-1} \text{ K}^{-1}$  at 300 K).

Fig. 5 presents the centerline solid- and gas-phase temperature profiles for the adiabatic and non-adiabatic absorber lateral wall conditions. Both sets of the profiles are qualitatively similar. For the non-adiabatic condition, the centerline gas and solid temperatures at the receiver outlet section ( $x = L_{\text{abs}}$ ) are about 200 K below the corresponding temperatures for the adiabatic receiver. (The difference is even higher [about 291 K] considering the radial average outlet gas temperatures for both cases.) Strikingly, the maximum solid and gas temperatures observed for the non-adiabatic condition are higher than the corresponding maximum temperatures for the adiabatic condition — *i.e.*, the absorber with higher heat losses is the same that achieves higher temperatures. This outcome is promoted by the effect of temperature on gas thermophysical properties, and consequently, on the velocity distribution. Fig. 6 shows velocity streamlines for both absorber lateral wall conditions. Since a fluid region is considered upstream the absorber (entry region) — in such a way that solved scalar gradients are negligible at the inlet section and first-type boundary conditions can be safely applied to governing equations featuring diffusive transport mechanisms [43] —, the incoming flow adapts to downstream conditions even before reaching the absorber front section. Consequently, the flow preferentially bypasses the absorber hot (central) region through the much colder region in the vicinity of the walls — see Fig. 6. This preferential (lower resistance) flow path is observed for both absorber lateral wall conditions but it is much more meaningful for the non-adiabatic absorber lateral wall condition — see in Fig. 6 the curvature of the streamlines at the absorber front section for both lateral wall conditions. For the non-adiabatic condition, lower gas velocity values near the centerline — mainly due to the flow bypassing this region — lead to lower interphase heat transfer rates (higher convection heat transfer resistance between phases), and consequently, higher solid temperatures. The maximum gas-phase temperature for the non-adiabatic condition is also higher than for the adiabatic condition due to the lower gas velocities that lead to higher residence times. (The higher maximum temperatures registered for the non-adiabatic condition are also supported by the diffusive [and radiative] heat transport mechanisms that are unable to flat the temperature distributions.) Therefore, lateral wall power losses promote an increase in the maximum temperatures (observed at the receiver centerline and near the front section) and a decrease in the minimum temperatures along the radial direction (at the absorber lateral wall) and along the longitudinal direction (at the absorber outlet section) — *i.e.*, the uniformity of the absorber temperature distribution deteriorates if lateral wall power losses are observed.

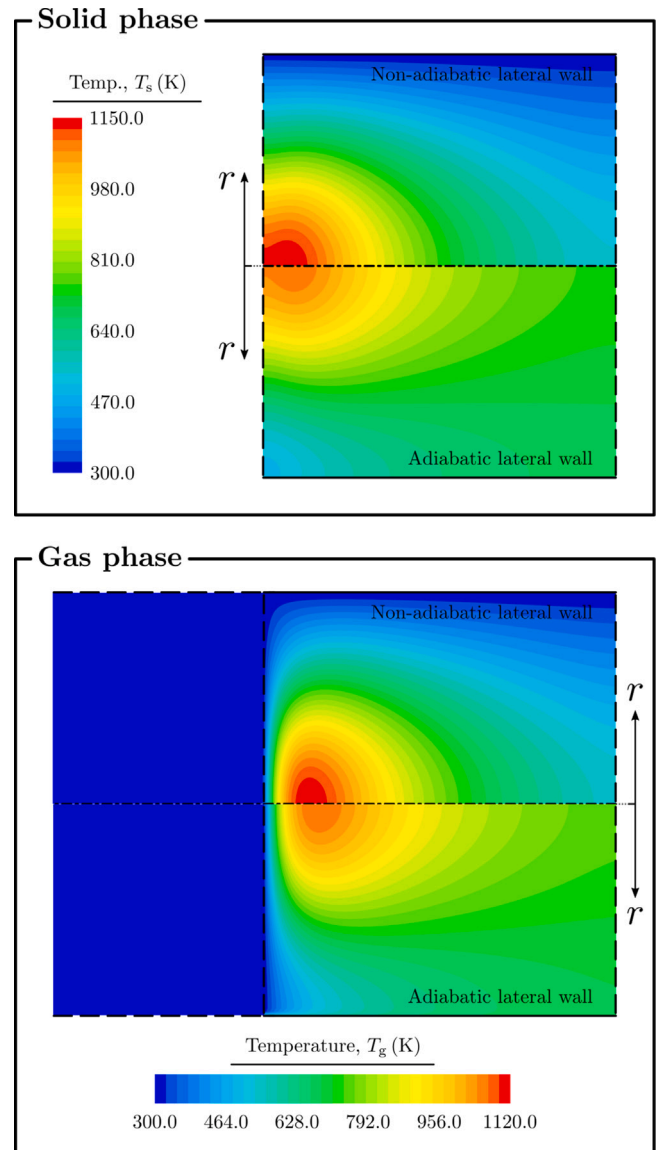


Fig. 4. Solid-phase temperature distribution (top) and gas-phase temperature distribution (bottom) computed considering adiabatic and non-adiabatic absorber lateral walls.

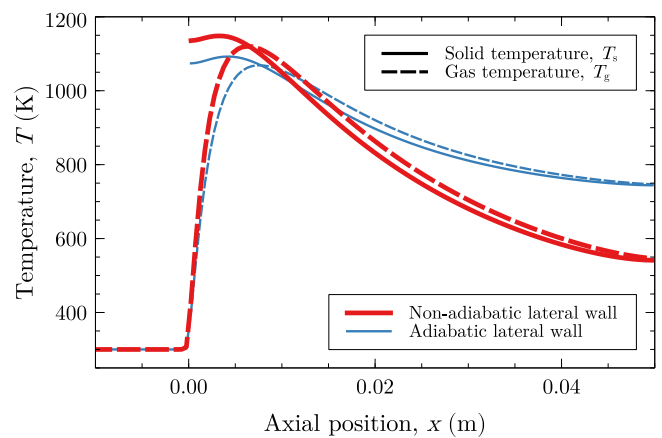


Fig. 5. Temperature profiles at the receiver centerline for the adiabatic and non-adiabatic absorber lateral wall conditions.

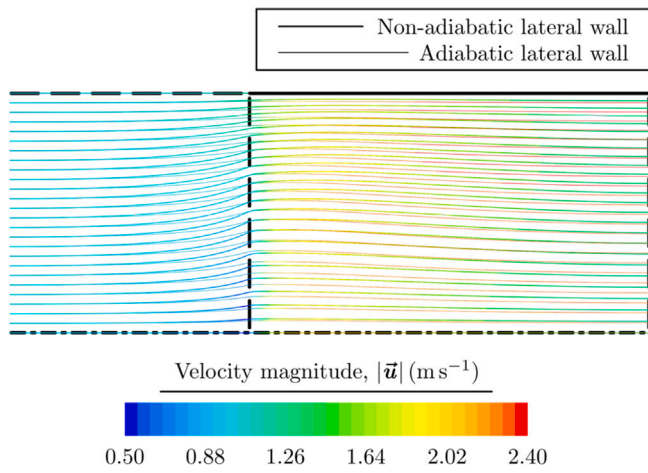


Fig. 6. Streamlines with the velocity magnitude for the adiabatic and non-adiabatic absorber lateral wall conditions.

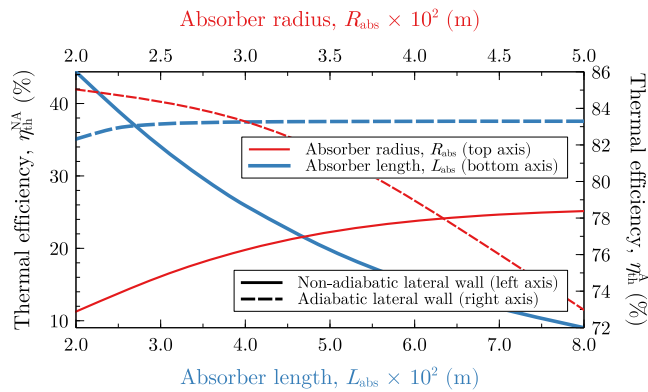


Fig. 7. Effect of absorber dimensions (radius and length) on the thermal efficiency for the adiabatic and non-adiabatic absorber lateral wall conditions.

#### 4.1.1. Effect of absorber dimensions

The effect of the absorber length and radius on the absorber lateral wall heat losses and overall thermal performance is herein investigated. Fig. 7 presents the thermal efficiency for both adiabatic and non-adiabatic absorber lateral wall conditions considering different absorber lengths (ranging from 2 to 8 cm) and different absorber radius values (ranging between 2 and 5 cm). Fig. 8 presents the relative power loss contribution of the lateral wall ( $P_{loss}^{latWall}/P_{loss}^{tot}$ ) — only relevant for the non-adiabatic condition — for the absorber length and radius values considered in Fig. 7. By varying the absorber radius, the total concentrated solar power provided to the receiver ( $Q_0$ ) is also changed. Therefore, to study the effect of the absorber radius, the ratio  $Q_0/\dot{m}$  — where  $\dot{m} (\equiv \pi R_{abs}^2 \rho_g u_{in})$  corresponds to the total mass flow rate — was kept constant and equal to the value computed with the reference values. Thus, an increase in the absorber radius implies simultaneously an increase in the total power provided to the receiver and a consistent decrease in the inlet gas velocity — note that according to the stated conditions:  $u_{in} \approx -9.998 \times 10^{-4} R_{abs}^{-2} [\exp(-2560 R_{abs}^2) - 1]$  m s<sup>-1</sup>, with  $R_{abs}$  provided in meters.

Fig. 7 shows that increasing the absorber length the thermal efficiency for the non-adiabatic wall condition decreases significantly — and moves away from the adiabatic thermal efficiency profile that becomes length-independent. The thermal efficiency decrease as the length is increased for the non-adiabatic wall condition is justified by the increase in the available lateral wall surface area through which heat losses occur — note that the relative power loss contribution of the lateral wall increases with the absorber length (see Fig. 8). For an

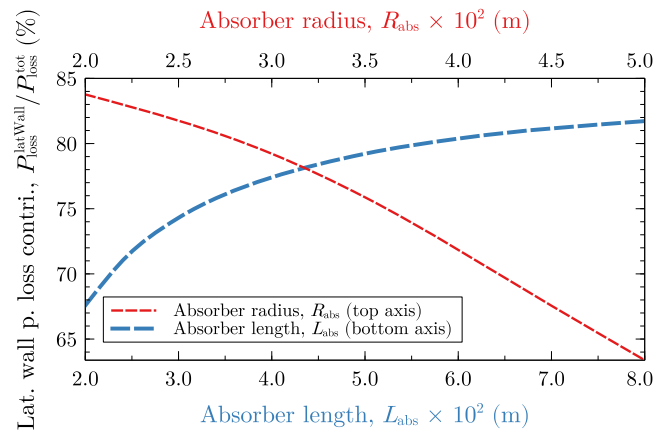


Fig. 8. Effect of absorber dimensions (radius and length) on the power loss contribution from the lateral wall (non-adiabatic absorber lateral wall condition).

adiabatic lateral wall, the effect of the absorber length is only relevant for low values (below 3 cm) for which the thermal efficiency is slightly reduced upon decreasing the absorber length. This evidence is due to the increasing relevance of thermal emission power losses through the absorber outlet section on the total power loss as the absorber length is decreased — note that relative transmission power losses are negligible, even for the lowest length considered ( $P_{loss}^{trans}/Q_0$  is about 0.25% for  $L_{abs}$  equal to 2 cm).

Regarding the absorber radius, Fig. 7 shows that as the absorber radius is increased the thermal efficiency decreases for the adiabatic condition and increases for the non-adiabatic condition. For the adiabatic condition, the stated trend observed upon increasing the absorber radius is due to the progressively lower convection heat transfer rates that arise as a consequence of decreasing the inlet gas velocity. Accordingly, solid temperatures at the vicinity of absorber front surface increase and heat losses by radiation take advantage — note that convective and radiative heat transport mechanisms are in competition for the absorbed concentrated solar radiation by the solid foam matrix. For the non-adiabatic condition, the reduction of convection heat transfer rates upon increasing the absorber radius is also observed — which deteriorates the thermal efficiency — but moving the lateral wall away from the centerline region where very high temperatures are observed (*i.e.*, increasing the absorber radius) overlaps the former effect along the radius range considered and the thermal efficiency is enhanced. In agreement, Fig. 8 reveals that the power loss contribution through the lateral surface to the total power loss diminishes as the absorber radius is increased, suggesting that energy losses through the absorber front section become more significant with an increasing absorber radius — since transmission losses and power losses through the outlet section are negligible.

#### 4.1.2. Effect of absorber geometrical parameters and thermophysical properties

The foam porosity ( $\phi$ ) and cell diameter ( $d_c$ ) are the absorber geometrical parameters under consideration. For the receiver thermophysical properties, the bulk (intrinsic) solid thermal conductivity ( $\lambda_s$ ), foam surface emissivity ( $\epsilon$ ), and lateral wall internal surface emissivity ( $\epsilon_{w,int}$ ) are considered. Figs. 9(a) and 9(b) present the thermal efficiency for both adiabatic and non-adiabatic absorber lateral wall conditions computed with different values for the absorber geometrical parameters and thermophysical properties, respectively. Fig. 10 presents the relative power loss contribution of the lateral wall for the cases considered in Figs. 9(a)–(b).

For the adiabatic condition, Fig. 9(a) shows that as the porosity increases (from the lowest value considered) the thermal efficiency increases as well reaching a maximum at about 0.925 and then decreases.

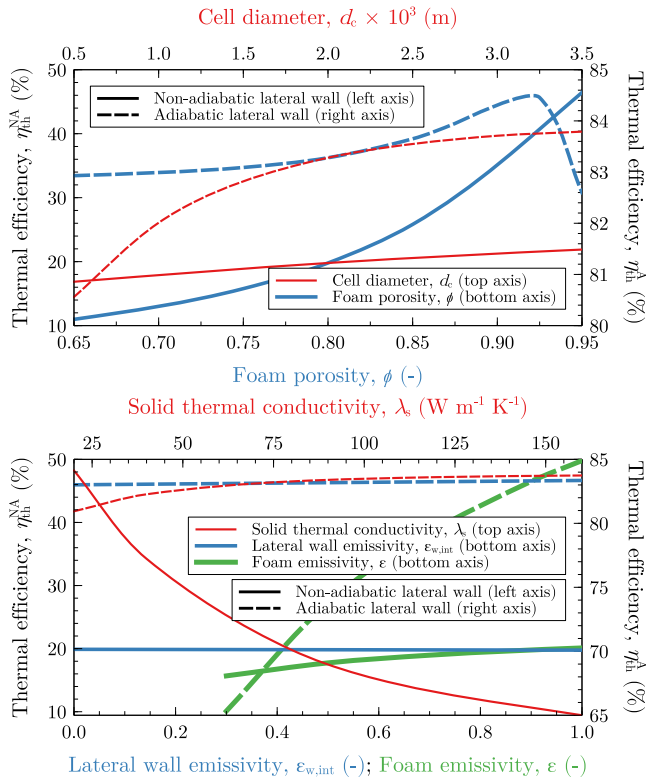


Fig. 9. Effect of absorber geometrical parameters (a) and thermophysical properties (b) on the thermal efficiency for the adiabatic and non-adiabatic absorber lateral wall conditions.

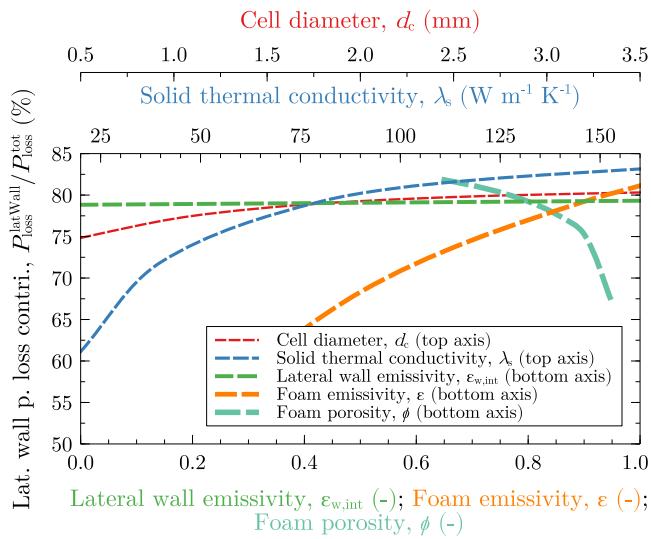


Fig. 10. Effect of absorber geometrical parameters and thermophysical properties on the power loss contribution from the lateral wall (non-adiabatic absorber lateral wall condition).

As the porosity is increased, radiative power losses through the inlet section decrease — since the concentrated solar irradiation distribution within the absorber ( $G_c$ ) becomes more uniform — and an increasing trend is simultaneously observed for: (i) radiative power losses through the outlet section — radiation emitted from the absorber internal pore structure; and (ii) transmission (concentrated solar) power losses. (Particularly, increasing the porosity from 0.90 to 0.95 the relative transmission power loss ( $P_{loss}^{trans} / Q_0$ ) increases from about 0.06% to

about 2.35%.) This tradeoff is responsible for promoting the stated maximum on the thermal efficiency profile. Literature studies on the effect of porosity — available for porosity values up to about 0.90 and considering adiabatic absorber lateral walls — are in full agreement with the reported trend on thermal efficiency (and total heat losses) — see Refs. [26,27,30,32,85]. (A similar maximum for the thermal efficiency varying the porosity is reported in Ref. [39].) Regarding the effect of the porosity on the absorber performance for the non-adiabatic condition, Fig. 9(a) shows that the thermal efficiency increases progressively from about 11% to about 46% as the porosity is increased from 0.65 to 0.95. This trend is a result of a decreasing contribution of heat losses through the lateral wall as the porosity increases — as suggested by Fig. 10. This is justified by a decrease in the effective solid thermal conductivity as the porosity is increased (see Eq. (8)) which results in lower conduction heat transfer rates to the lateral wall — note that heat conduction from the absorber solid phase to the lateral wall is the most relevant lateral wall power loss contribution.

Regarding the cell diameter, Fig. 9(a) shows that as the cell diameter increases the thermal efficiency for both lateral wall conditions also increases. (For the adiabatic absorber lateral wall condition, the reported thermal efficiency trend upon increasing the cell diameter is in line with the literature [27,30,60,70,85].) This is mainly due to the fact that increasing the cell diameter the extinction and absorption coefficients — computed with Eqs. (21) and (19), respectively — decrease which promotes a more uniform distribution and absorption of concentrated solar radiation within the absorber volume [29,93]. (For very low cell diameter values, the extinction coefficient is very high and the solar radiation penetration dept is very low — solar radiation is only available near the vicinity of the irradiated section and at very high power values. As a consequence, very high solid-phase temperatures establish at the receiver inlet section which contributes to increase the radiative power losses and reduce the receiver thermal efficiency.) Note that the cell diameter also affects the interphase momentum and heat transport rates (source terms of the momentum and energy balance equations) but to a lower extent on the overall receiver thermal performance (thermal efficiency) in comparison to the effect of the cell diameter on radiative heat transport rates. Along the range considered in this study for the cell diameter, the relative transmission and radiation emission losses through the receiver outlet section are negligible ( $(P_{loss}^{trans} + P_{loss}^{out}) / Q_0 < 0.1\%$ ) and thus energy losses are only significant through the fluid entrance section and lateral wall — the later contribution is available only for the non-adiabatic absorber lateral wall condition. For the non-adiabatic condition, Fig. 10 shows that the contribution of heat losses through the absorber lateral wall on the receiver total power loss slightly increases upon increasing the cell diameter due to a relevant decrease of power losses through the absorber inlet section.

Contrarily to the absorber geometrical parameters that affect simultaneously several transport mechanisms, the thermophysical properties herein investigated only affect a specific (heat) transport mechanism. Therefore, the role of such properties on the overall thermal behavior for both lateral wall conditions is much more straightforward to analyze. In particular, the solid thermal conductivity only influences heat diffusion rates in the absorber solid phase. Fig. 9(b) shows that an increase in the solid thermal conductivity results in a different thermal efficiency trend for the two wall conditions. For the adiabatic condition, an increase in the solid thermal conductivity promotes a slight increase in the thermal efficiency. The reported effect of the intrinsic solid thermal conductivity is in full agreement with results available in the literature [62,65,83]. (Nevertheless, note that the particular effect of the intrinsic solid thermal conductivity on the thermal efficiency depends on the actual combination of the geometrical parameters, thermophysical properties, and operating conditions under consideration, as well as on the range considered for the thermal conductivity [27,37].) The thermal efficiency slight increase upon increasing the solid thermal conductivity is observed because an increase

in the solid thermal conductivity contributes to decrease the highest solid temperatures (flattening the solid temperature distribution) avoiding very high solid temperatures, and consequently, high radiative power losses to the surrounding environment through the inlet and outlet sections. However, for the non-adiabatic condition an increase in the solid thermal conductivity also contributes (in a more significant extent) to increase conduction heat losses to the lateral wall — note in Fig. 10 the increasing relevance of lateral wall heat losses on the total power loss as the solid thermal conductivity increases. Therefore, an increase in the solid thermal conductivity results in a dramatic thermal efficiency decrease for the non-adiabatic lateral wall condition.

Concerning the foam emissivity, Fig. 9(b) shows that regardless of the absorber lateral wall condition the highest possible value for the foam emissivity is recommended to achieve a high thermal efficiency. This evidence is in line with literature results [52,61]. Particularly for the adiabatic condition, a significant increase in the thermal efficiency (about 20 percentage points [pp]) is observed increasing the foam emissivity from 0.3 to the maximum theoretical value. For the non-adiabatic condition, although the total power losses decrease while increasing the foam emissivity (as supported by the slight increase in the thermal efficiency), the heat losses through the lateral wall increase — see Fig. 10. An increase in the foam emissivity promotes higher absorption rates of solar radiation (since the absorption coefficient increases) for an identical solar irradiation distribution within the absorber (given by Eq. (11)) — note that the extinction coefficient required in Eq. (11) is independent of the foam emissivity. Backscattering losses through the inlet section are decreased as the foam emissivity is increased.

Finally, the lateral wall internal surface emissivity plays a particular role on the receiver operation through the Marshak's boundary condition — see Eq. (31). Fig. 9(b) shows a modest increase of the thermal efficiency for the adiabatic condition and a negligible decrease of the thermal efficiency for the non-adiabatic condition upon increasing the lateral wall emissivity. In accordance, the relevance of the lateral wall heat losses on the total power loss from the receiver increases almost imperceptibly (less than 1 pp) as the lateral wall emissivity increases from 0.0 to 1.0 — see Fig. 10. The insignificant role of the lateral wall emissivity on the overall absorber thermal performance is due to the reference combination of absorber dimensions, geometrical parameters, and thermophysical properties that particularly lead to high optical thickness values hampering high rates of heat transfer by radiation from high-temperature regions to the absorber lateral surface.

#### 4.1.3. Effect of operating conditions

The inlet gas velocity ( $u_{in}$ ) and the concentrated solar radiation flux profile — fully defined by parameters  $A$  and  $B$  (see Eq. (12)) — are the receiver operating variables herein investigated. Fig. 11 presents the thermal efficiency for both adiabatic and non-adiabatic absorber lateral wall conditions considering different inlet gas velocities and different parameters  $A$  and  $B$ . (Fig. 11 presents results for parameters  $A$  and  $B$  varying freely and, additionally, for parameter  $B$  correlated with parameter  $A$  in such a way that the total concentrated solar power provided to the receiver is kept constant and equal to the reference value.) Fig. 12 presents the relative power loss contribution of the lateral wall for the cases considered in Fig. 11.

Fig. 11 shows that an increase in the inlet gas velocity promotes an increase of the receiver thermal efficiency independently of the absorber lateral wall condition. For the adiabatic condition, a significant increase of thermal efficiency (about 23 pp) is observed increasing the inlet gas velocity from the lowest to the highest considered values. A further increase in the inlet velocity continues to improve the thermal efficiency for the adiabatic condition but at a much lower pace. (These results are in full agreement with the literature [26,39,52,60,63].) For the non-adiabatic condition, a dramatic increase of the thermal efficiency is observed along the entire inlet velocity range considered. Moreover, the results suggest that the thermal efficiency of the non-adiabatic absorber would continue to increase at a significant rate

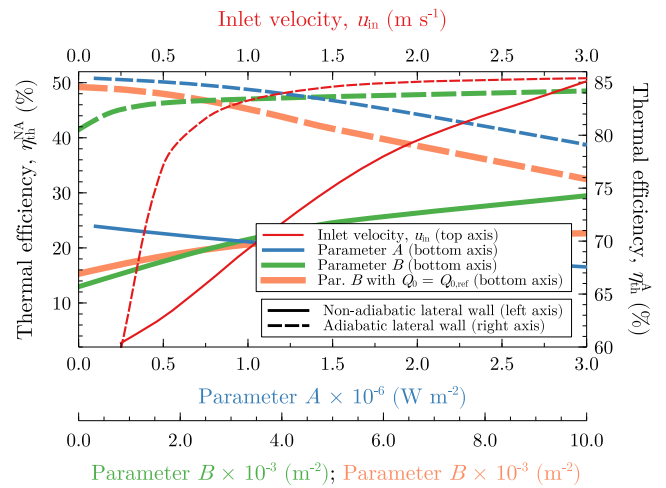


Fig. 11. Effect of receiver operating conditions (inlet gas velocity and concentrated solar irradiation profile) on the thermal efficiency for the adiabatic and non-adiabatic absorber lateral wall conditions.

if the inlet gas velocity were increased beyond the maximum value considered. The increase in thermal efficiency registered for both absorber lateral wall conditions upon increasing the inlet velocity is due to the promotion of convection heat transfer rates — concentrated solar power captured by the solid phase is preferentially transported to the bulk fluid phase (due to an increase in the convection heat transfer coefficients) instead of being lost by re-radiation through the inlet section (and by conduction and radiation to the absorber lateral wall for the non-adiabatic condition). Although heat losses through the inlet section and lateral wall decrease as the inlet gas velocity increases, Fig. 12 shows a maximum for the relative contribution of lateral wall power losses at about  $0.85 \text{ m s}^{-1}$ . Below (above) this value, an increase of the inlet velocity results in a higher (lower) decrease of energy losses through the inlet than the decrease of the energy loss through the lateral wall. Therefore, increasing the velocity from low values is particularly effective in reducing the heat losses through the inlet section while a reduction of power losses through the lateral wall is particularly significant increasing the velocity from medium values ( $u_{in} \gtrsim 0.85 \text{ m s}^{-1}$ ). (Although not shown, the increase of the thermal efficiency as the velocity is increased results in lower average outlet gas temperatures due to the decrease of the gas residence time in the absorber.)

Regarding the role of parameters  $A$  and  $B$  when varied freely, Fig. 11 shows that an increase of  $A$  or a decrease of  $B$  deteriorates the thermal efficiency for both lateral wall conditions — even though the average outlet gas temperature increases (not shown). As parameter  $A$  is increased (or parameter  $B$  is decreased), the total solar power supplied to the absorber increases which results in higher rates of solar radiation absorption, higher solid temperatures, and ultimately, higher radiative power losses through the receiver inlet section — lower thermal efficiency values. (The current results for the adiabatic absorber lateral wall condition are in full agreement with the literature [33,94].) However, if the total concentrated solar power is kept constant — and equal to the reference value ( $Q_0 = Q_{0,ref}$ ) — and considering the adiabatic condition, a decrease of parameter  $B$  which implies a consistent decrease of parameter  $A$  leads to a contrary trend on the thermal efficiency to that concluded for a freely varied parameter  $B$  — under such conditions the thermal efficiency for the adiabatic condition increases upon decreasing the parameter  $B$ . This is observed because as parameter  $B$  is decreased the concentrated solar flux profile becomes more uniform for the same total power. For the non-adiabatic condition, Fig. 12 shows that the relevance of heat losses through the lateral wall on the total power loss decreases as the value

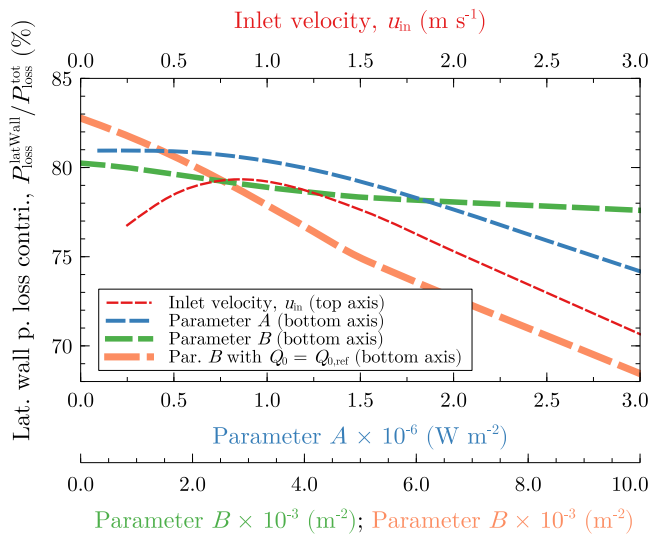


Fig. 12. Effect of operating conditions (inlet gas velocity and concentrated solar irradiation profile) on the power loss contribution from the lateral wall (non-adiabatic absorber lateral wall condition).

of  $A$  increases. This evidence means that the increase of power losses through the inlet section becomes more relevant than the increase of heat losses through the lateral wall as parameter  $A$  is increased. (Note that emission and transmission power losses through the outlet section are negligible for the cases under consideration.) Regarding parameter  $B$ , either freely varied or correlated with parameter  $A$ , Fig. 12 shows that the relative power loss through the absorber lateral wall decreases as the value of parameter  $B$  is increased — *i.e.*, as the concentrated solar flux profile becomes more non-uniform for a constant maximum value at the receiver centerline (parameter  $B$  varying freely) or for a constant total power (parameter  $B$  correlated with parameter  $A$ ). This is observed because as parameter  $B$  is increased (freely or correlated) lower concentrated solar flux values are provided near the absorber lateral wall. The decrease of the relative power loss through the lateral wall is more remarkable as parameter  $B$  is increased correlated with parameter  $A$  because power losses through the inlet section increase more remarkably than power losses through the lateral wall. (Note that as the correlated parameter  $B$  is increased solar flux values at the absorber central region [near the centerline] must increase to compensate the solar flux decrease near the lateral wall — in order to keep constant the total power provided to the receiver.)

#### 4.2. Effect of external heat transfer conditions

The receiver external heat transfer conditions herein investigated are established by defining a particular value for: (i) the convection heat transfer coefficient at the receiver external lateral wall ( $h$ ); and (ii) the external surface emissivity of the receiver lateral wall ( $\epsilon_{w,ext}$ ). These parameters control convection and radiation heat losses from the external surface of the receiver lateral wall. (The external [environment] fluid and surrounding surface temperatures are both fixed at 300 K.) An insulation layer between the absorber porous region and the external environment is not applied ( $\delta_{ins} = 0$  in Eqs. (33) and (35)). Therefore, differences on the receiver thermal performance in relation to the performance obtained with an adiabatic absorber lateral wall condition are solely due to the role of external heat transfer conditions. In this study, the reference values previously stated for the absorber dimensions, absorber geometrical parameters, absorber thermophysical properties, and operating conditions are considered.

Fig. 13 presents the effect of the lateral wall external surface emissivity and convection heat transfer coefficient on the receiver thermal

efficiency and average lateral wall temperature. In this figure, the individual (exclusive) effect of emissivity and convection heat transfer coefficient can be observed. The single effect of surface emissivity on the thermal efficiency and average lateral wall temperature is observed considering a negligible convection heat transfer coefficient and varying the emissivity between its theoretical limits. In addition, multi-mode (combined) heat loss conditions (mixed convection and radiative heat loss mechanisms) are also presented for emissivity values equal to 0.5 and 1.0. The range considered for the convection heat transfer coefficient takes into account typical values for gases under the free (natural) convection regime ( $2\text{--}25 \text{ W m}^{-2} \text{ K}^{-1}$ ) and forced convection conditions ( $25\text{--}250 \text{ W m}^{-2} \text{ K}^{-1}$ ).

Fig. 13 shows a progressive decrease of the receiver thermal efficiency and lateral wall temperature as the convection heat transfer coefficient increases. This is observed independently of the surface emissivity value. Such a decrease is slightly more accentuated for lower convection coefficients and lower surface emissivity values. Neglecting convection heat losses and increasing the surface emissivity between 0.0 and 1.0 the receiver thermal efficiency decreases from its adiabatic absorber lateral wall value (83.3%) to approximately 79.0%. This reduction of about 4.3 pp on the thermal efficiency (corresponding to about 71.2 W) is the maximum possible difference while varying only the surface emissivity between the corresponding theoretical limits for any convection heat transfer coefficient value. This is observed because the effect of external surface emissivity (lateral wall radiative heat losses) on the thermal efficiency is limited and becomes less relevant as the convection heat transfer coefficient increases. (Note that in Fig. 13 as the convection heat transfer coefficient is increased the difference between the thermal efficiency profiles for emissivity values equal to 0.0 and 1.0 decreases. Particularly, for a convection coefficient equal to  $250 \text{ W m}^{-2} \text{ K}^{-1}$  the thermal efficiency decreases from 55.4% to 54.4% [only about 1 pp] as the surface emissivity is increased from 0.0 to 1.0.) For a particular surface emissivity value, as the convection coefficient is increased the surface temperature of the lateral wall decreases and the corresponding radiative heat transfer coefficient also decreases. Therefore, an increase in the convection coefficient leads to a decrease in the relevance of radiative heat losses (and in the importance of the actual surface emissivity value) on the receiver thermal performance. (Similarly, an increase in the surface emissivity — which promotes an increase in the radiative heat transfer coefficient — leads to a decrease in the relevance of convection heat losses [and in the importance of the actual convection heat transfer coefficient] on the receiver thermal performance. This is concluded in Fig. 13 by a smoother decrease of the thermal efficiency with the convection coefficient for higher surface emissivity values.) This is observed because convection and radiative heat transport mechanisms are competing for the same power available at the receiver lateral wall. It is worth mentioning that for all external heat transfer conditions herein considered, the total power loss through the absorber front section remains approximately constant —  $P_{loss}^{in}/Q_0 \approx 16.6\%$ . (This evidence was not observed in Section 4.1 while varying the absorber internal parameters and properties and operating conditions.) This means that the actual external heat transfer conditions at the lateral wall do not affect radiative heat losses from the front absorber section.

Fig. 14 presents the solid- and gas-phase temperature distributions for two combined convection–radiation external heat transfer conditions with a surface emissivity equal to 1.0 and convection heat transfer coefficients equal to  $5 \text{ W m}^{-2} \text{ K}^{-1}$  (low value within the natural convection regime) and  $250 \text{ W m}^{-2} \text{ K}^{-1}$  (upper limit of the forced convection regime). The highest and lowest gas- and solid-phase temperatures are both registered for the higher convection coefficient case. (This evidence is aligned with the findings presented in Section 4.1 according to which temperature fields become more non-uniform in the presence of lateral wall heat losses.) In relation to the adiabatic absorber lateral wall condition, the thermal efficiency is reduced in 5.0 and 28.8 pp for the lowest and highest convection heat transfer coefficients under

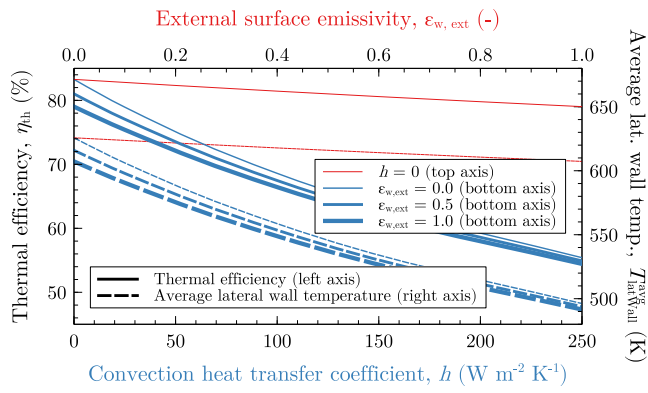


Fig. 13. Effect of the lateral wall external surface emissivity and convection heat transfer coefficient on the receiver thermal efficiency and average lateral wall temperature.

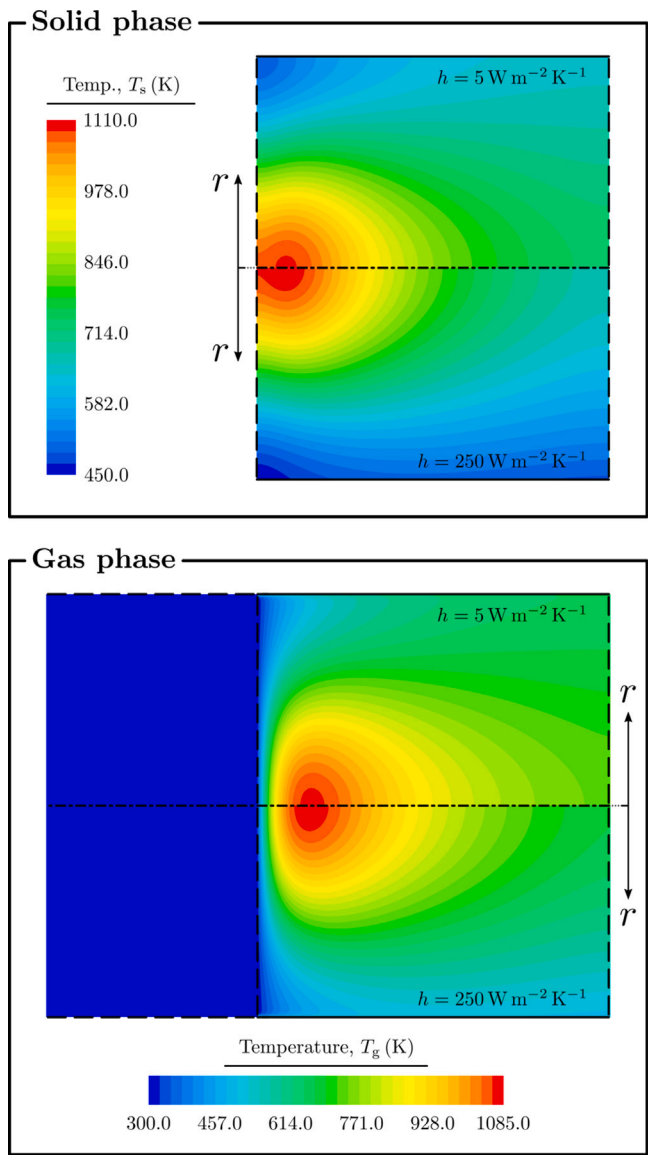


Fig. 14. Solid-phase temperature distribution (top) and gas-phase temperature distribution (bottom) computed considering the convection heat transfer coefficient at the non-insulated receiver lateral wall equal to  $5.0 W m^{-2} K^{-1}$  and  $250.0 W m^{-2} K^{-1}$  with an external surface emissivity of the receiver lateral wall equal to unity ( $\epsilon_{w,ext} = 1.0$ ).

consideration — i.e., the lateral wall power losses account for about 82.8 W and 477.2 W, respectively.

An average convection heat transfer coefficient suitable for the natural convection regime between the external surface of the receiver lateral wall and the adjoining quiescent fluid medium (stationary air) can be estimated based on the Nusselt number correlation provided by Churchill and Chu [95]. This correlation is reasonable for the current absorber placed in the horizontal position and with a constant external surface temperature. Under such conditions and assuming a surface emissivity equal to 1.0 (black surface), the convection heat transfer coefficient is approximately equal to  $8.8 W m^{-2} K^{-1}$  — for an average absorber lateral wall temperature approximately equal to 601.2 K (in full agreement with the correspondence between the convection coefficient and average lateral wall temperature presented in Fig. 13). According to Fig. 13, this external heat transfer condition results in a thermal efficiency of about 77.7%, which corresponds to a decrease of about 5.6 pp in relation to the adiabatic absorber lateral wall value. For the forced convection regime, the Nusselt number correlation provided by Churchill and Bernstein [96] that is suitable for the absorber in cross flow with air can be applied to estimate the average convection heat transfer coefficient. Therefore, for a wind velocity equal to  $20 m s^{-1}$  and the absorber lateral wall external surface emissivity equal to 1.0, the convection heat transfer coefficient is approximately equal to  $70.7 W m^{-2} K^{-1}$  — for an average absorber lateral wall temperature approximately equal to 563.8 K (in full agreement with Fig. 13). According to Fig. 13, this external heat transfer condition results in a thermal efficiency of about 69.6%, which corresponds to a decrease of about 13.7 pp in relation to the adiabatic absorber lateral wall value. (The previous convection coefficients for free and forced convection regimes were estimated neglecting border effects particularly near the inlet section, as well as the shear-driven flow due to the external air suction at the absorber inlet section. Moreover, required temperature-dependent air thermophysical properties at atmospheric pressure were gathered from Ref. [97].)

The prejudicial effect on the receiver thermal efficiency caused by lateral wall convective and radiative heat losses — even assuming a natural convection regime — shows the great relevance of an appropriate insulation layer application at the absorber lateral wall.

#### 4.3. Combined effects of insulation material, insulation thickness, and external heat transfer conditions

In this section, an insulation layer is applied onto the absorber lateral wall to investigate the corresponding effect on the receiver thermal performance. In particular, the effects of the insulation material thermal conductivity ( $\lambda_{ins}$ ) and insulation layer thickness ( $\delta_{ins}$ ) are analyzed under different external heat transfer conditions. The thermal performance of the insulation layer is predicted solving the two-dimensional Laplace equation — two-dimensional, steady-state form of Eq. (9) in cylindrical coordinates, with a constant thermal diffusion coefficient — subjected to the boundary and interface conditions given by Eqs. (37)–(39). The reference values for the absorber dimensions, absorber geometrical parameters, absorber thermophysical properties, and operating conditions are herein considered.

Figs. 15(a)–(c) present the effect of the insulation layer thickness, insulation thermal conductivity, and external heat transfer conditions on the receiver thermal efficiency. In these figures, three different thermal conductivity values are considered for the insulation material (0.1, 1.0, and  $10.0 W m^{-1} K^{-1}$ ) and the insulation layer thickness is varied from 0 to 0.1 m. Nine different external heat transfer conditions are considered — given by the combinations between three different convection heat transfer coefficients (0, 10, and  $100 W m^{-2} K^{-1}$ ) and three different surface emissivity values (0.0, 0.5, and 1.0). Figs. 15(a)–(c) show that the application of an insulation layer does not necessary lead to a reduction of power losses from the absorber lateral wall — i.e., the application of an insulation layer may result in a promotion

of lateral wall heat losses (decrease of the receiver thermal efficiency). Particularly, these figures show that applying an insulation layer made of a high thermal conductivity material results in a deterioration of the receiver thermal efficiency in relation to the case without any insulation layer — compare the results obtained with the highest thermal conductivity material ( $10 \text{ W m}^{-1} \text{ K}^{-1}$ ) against the results observed without applying any insulation layer ( $\delta_{\text{ins}} = 0$ ) for the same external conditions. This is due to the fact that two contrary effects on lateral wall heat losses are observed while increasing the thickness of the insulation layer: (i) the external surface area from which convection and radiation heat transfer is observed to the surrounding environment is increased — promoting an increase in heat losses; and (ii) the resistance to conduction heat transfer across the insulation layer increases — promoting a decrease of heat losses. For high insulation thermal conductivities (and low insulation thickness values), the former effect dominates and the receiver thermal efficiency decreases. (For one-dimensional heat conduction along the radial coordinate of a tubular [cylindrical] insulation layer, the two referred opposite effects lead to the well-known concept of critical radius — defined as the ratio between the thermal conductivity and the external overall heat transfer coefficient [ $r_c \equiv \lambda_{\text{ins}}/U_{\text{ext}}$ ]. Accordingly, if the absorber radius — that is equal to the insulation inner surface radius — were higher than the critical radius, the application of the insulation layer improves the thermal efficiency since heat losses are reduced. Otherwise, if the absorber radius were lower than the critical radius heat losses may or may not increase depending on the actual insulation thickness.) Assuming a one-dimensional heat conduction approximation, to observe a decrease of heat losses independently of the applied insulation thickness for external overall heat transfer coefficients ( $U_{\text{ext}}$ ) equal to  $10 \text{ W m}^{-2} \text{ K}^{-1}$  and  $100 \text{ W m}^{-2} \text{ K}^{-1}$  the insulation thermal conductivity should not be higher than  $0.3 \text{ W m}^{-1} \text{ K}^{-1}$  and  $3.0 \text{ W m}^{-1} \text{ K}^{-1}$ , respectively.

The application of an insulation layer is particularly effective in reducing lateral wall power losses under high convection heat transfer coefficients and high surface emissivity values — see in Fig. 15(c) the thermal efficiency profiles for the lowest thermal conductivity value according to which the thermal efficiency increases more expressively for the case with the highest convection coefficient than for the case with the lowest convection coefficient as the insulation thickness is increased. (For such external conditions [convection coefficient and surface emissivity equal to  $100 \text{ W m}^{-2} \text{ K}^{-1}$  and 1.0, respectively], a remarkable increase in the thermal efficiency from about 66.4% (naked absorber) to 80.0% is achieved applying only a 5 mm thick insulation layer with the lowest thermal conductivity [ $0.1 \text{ W m}^{-1} \text{ K}^{-1}$ ].)

For a particular insulation thickness and external heat transfer conditions, Figs. 15(a)–(c) show that as the insulation material thermal conductivity is decreased the receiver thermal efficiency is increased. Moreover, the relevance of the actual external heat transfer conditions on the receiver thermal efficiency is reduced as the insulation material thermal conductivity is decreased or as the insulation thickness is increased. In the limit of a negligible thermal conductivity, the absorber lateral wall is adiabatic and the actual external heat transfer conditions as well as the insulation thickness become irrelevant to the receiver thermal performance. On the other hand, the application of an extremely thick insulation layer with a finite thermal conductivity — in such a way that negligible heat losses from the insulation outer surface to the environment are observed — would not provide the same receiver performance as that obtained considering an adiabatic absorber lateral wall condition. While heat losses from the outer insulation surface are absent for an extremely thick insulation layer, the insulation layer may still support heat transport along the receiver longitudinal coordinate from high-temperature (downstream) regions to low-temperature (upstream) regions.

Fig. 16 presents the insulation layer temperature distribution for different insulation thermal conductivities, insulation thicknesses, convection heat transfer coefficients, and external surface emissivities. For the cases under consideration in Fig. 16, Figs. 17(a)–(b) present the

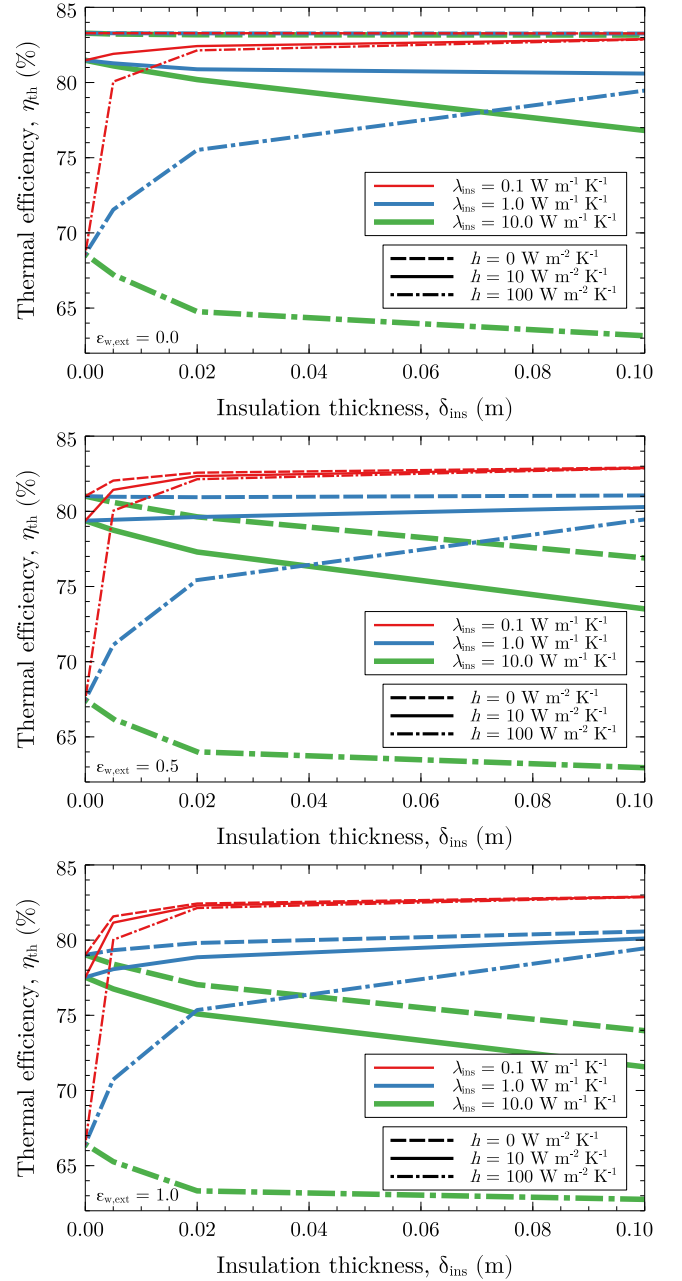
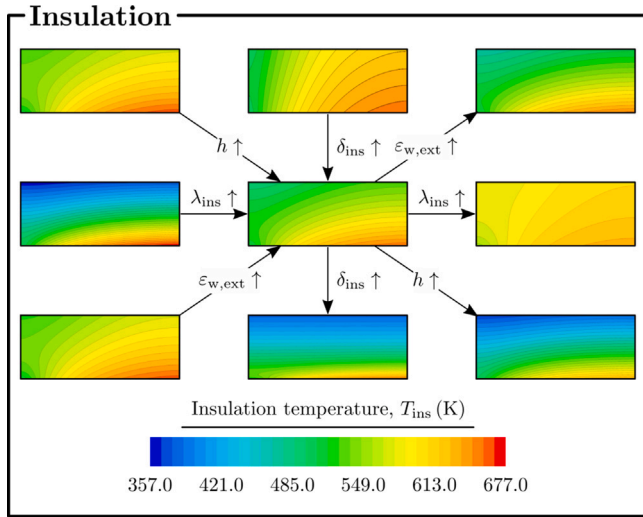


Fig. 15. Effect of the insulation thickness, insulation thermal conductivity, and external convection heat transfer coefficient on the receiver thermal efficiency for three lateral wall external surface emissivity values: (a) 0.0; (b) 0.5; and (c) 1.0. ((a), (b), and (c): top, middle, and bottom, respectively. This labeling scheme will apply throughout this document.).

radial heat flux profiles at the insulation layer inner surface ( $r = R_{\text{abs}}$ ) and outer surface ( $r = R_{\text{abs}} + \delta_{\text{ins}}$ ) along the receiver longitudinal coordinate, while Fig. 18 presents the relative lateral wall power loss, the relative power regain, and the inlet power loss difference. The power regain — power transferred from downstream absorber hotter regions to upstream absorber colder regions through the insulation layer — is calculated in accordance with Eq. (43).

$$P_{\text{regain}}^{\text{latWall}} = \int_A \mathbb{1}_{[|T_{\text{ins}} - \bar{T}| > 0]} \lambda_{\text{ins}} \nabla T_{\text{ins}} \cdot \vec{n} dA \quad (43)$$

Fig. 16 shows that a more uniform temperature distribution in the insulation layer is observed increasing the insulation thermal conductivity and decreasing the insulation thickness, convection heat transfer



**Fig. 16.** Effect of the insulation thermal conductivity, insulation thickness, convection heat transfer coefficient, and external surface emissivity on the insulation temperature distribution. Reference (mid) values:  $\lambda_{ins} = 1.0 \text{ W m}^{-1} \text{ K}^{-1}$ ;  $\epsilon_{w,ext} = 0.5$ ;  $\delta_{ins} = 0.02 \text{ m}$ ; and  $h = 10 \text{ W m}^{-2} \text{ K}^{-1}$ . Lowest/highest values:  $\lambda_{ins} = 0.1/10.0 \text{ W m}^{-1} \text{ K}^{-1}$ ;  $\epsilon_{w,ext} = 0.0/1.0$ ;  $\delta_{ins} = 0.005/0.1 \text{ m}$ ; and  $h = 0/100 \text{ W m}^{-2} \text{ K}^{-1}$ . (For ease of visualization, the case with an insulation thickness lower/higher than the reference value was stretched/compressed along the radial direction to match the reference insulation thickness.)

coefficient, and external surface emissivity. The isothermal lines show an increasing relevance of axial heat conduction in the insulation layer as the insulation thermal conductivity increases and as the convection heat transfer coefficient or external surface emissivity decreases. Figs. 17(a)–(b) and 18 show that local heat flux values and the total power loss at the insulation outer surface decrease with the decrease of the insulation thermal conductivity, external surface emissivity, and convection heat transfer coefficient. As the insulation thickness is increased, Figs. 17(b) and 18 also show a decrease of local heat flux values and total power loss at the insulation outer surface. (However, this trend is highly dependent on the ratio  $\lambda_{ins}/U_{ext}$  — as concluded before for thermal efficiency — and the opposite trend is registered if the highest thermal conductivity value were considered as the reference value [not shown].)

Figs. 17(a)–(b) show that the insulation is providing power to the absorber over a longer extent near the absorber front section for higher insulation thermal conductivities and insulation thicknesses and lower external surface emissivities and convection heat transfer coefficients. (In Figs. 17(a)–(b), power is being provided from the insulation layer back to the absorber where  $-q_r''(r = R_{abs}, x) > 0$ .) Accordingly, Fig. 18 shows that the power regain and inlet power loss increase by decreasing the convection coefficient or surface emissivity — i.e., by increasing the lateral wall external thermal resistance ( $\equiv 1/U_{ext}$ ). Note that the power regain and the lateral wall power loss are competing against each other for the same source of power. Therefore, if the thermal resistance between the insulation outer surface and the external environment increases (by decreasing the convection coefficient or surface emissivity) the power regain is benefited. As the thermal conductivity increases the power regain also increases, while the inlet power loss may decrease (for high values of  $\delta_{ins} U_{ext}/\lambda_{ins}$ ) or increase (for low values of  $\delta_{ins} U_{ext}/\lambda_{ins}$  as shown in Fig. 18). Regarding the insulation thickness, two different behaviors are observed while increasing the insulation thickness: (i) if lateral wall power losses are decreasing (or are negligible) the power regain increases (case shown in Figs. 17(b) and 18) or remains negligible (not shown) and the power losses through the inlet increases; or (ii) if lateral wall power losses are being promoted the power regain and inlet power losses may increase (for small thickness values) — benefiting from the increase of the insulation cross-sectional area — or decrease if power losses to the environment lead

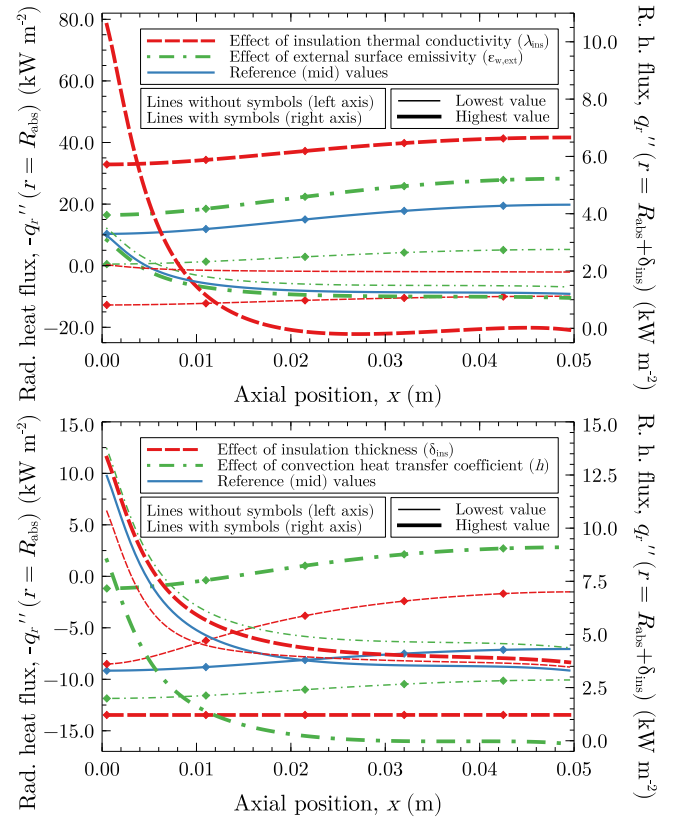


**Fig. 17.** Effect on the radial heat flux profiles at the insulation inner surface (left axis) and outer surface (right axis) of the insulation thermal conductivity and external surface emissivity (a) and insulation thickness and convection heat transfer coefficient (b). Reference (mid) values:  $\lambda_{ins} = 1.0 \text{ W m}^{-1} \text{ K}^{-1}$ ;  $\epsilon_{w,ext} = 0.5$ ;  $\delta_{ins} = 0.02 \text{ m}$ ; and  $h = 10 \text{ W m}^{-2} \text{ K}^{-1}$ . Lowest/highest values:  $\lambda_{ins} = 0.1/10.0 \text{ W m}^{-1} \text{ K}^{-1}$ ;  $\epsilon_{w,ext} = 0.0/1.0$ ;  $\delta_{ins} = 0.005/0.1 \text{ m}$ ; and  $h = 0/100 \text{ W m}^{-2} \text{ K}^{-1}$ .

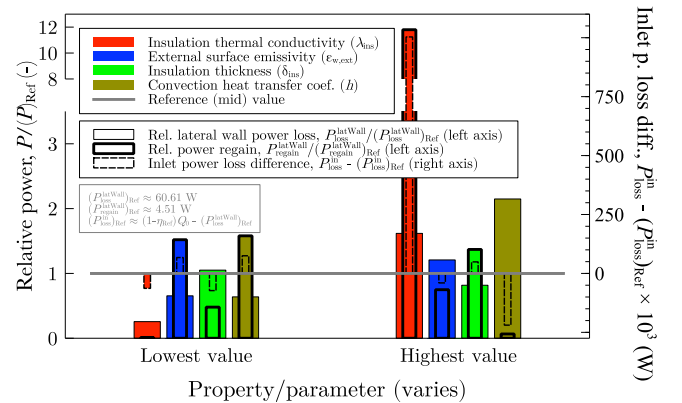


**Fig. 18.** Effect of the insulation thermal conductivity, insulation thickness, external surface emissivity, and convection heat transfer coefficient on the relative lateral wall power loss, relative power regain, and inlet power loss difference. Reference (mid) values:  $\lambda_{ins} = 1.0 \text{ W m}^{-1} \text{ K}^{-1}$ ;  $\epsilon_{w,ext} = 0.5$ ;  $\delta_{ins} = 0.02 \text{ m}$ ; and  $h = 10 \text{ W m}^{-2} \text{ K}^{-1}$ . Lowest/highest values:  $\lambda_{ins} = 0.1/10.0 \text{ W m}^{-1} \text{ K}^{-1}$ ;  $\epsilon_{w,ext} = 0.0/1.0$ ;  $\delta_{ins} = 0.005/0.1 \text{ m}$ ; and  $h = 0/100 \text{ W m}^{-2} \text{ K}^{-1}$ .

to a significant reduction of the absorber lateral wall temperature (not shown).

Among all combinations considered in Figs. 15(a)–(c), the highest power regain (approximately equal to 89.37 W) is observed for the case with the highest insulation thermal conductivity ( $10 \text{ W m}^{-1} \text{ K}^{-1}$ ), highest insulation thickness (0.1 m), and convection coefficient and surface emissivity equal to zero. (This is in full accordance with the effect

of insulation thickness, insulation thermal conductivity, and external heat transfer conditions on the power regain as previously stated.) The absorber performance for this particular combination of insulation parameters and properties and external heat transfer conditions can be readily compared with the reference case of the adiabatic absorber lateral wall to conclude about the role and relevance of the power regain. Therefore, Fig. 19 presents the solid temperature distributions for the highest power regain case and the adiabatic absorber lateral wall condition. Fig. 19 shows that the power regain promotes an increase of solid temperatures, particularly at the absorber top-front region (up to 70 K at the absorber lateral wall) at the expense of a slight decrease of temperatures at the absorber top-rear region (up to 16 K observed at the absorber lateral wall near the receiver exit section). Therefore, the power regain is indirectly responsible for a slight increase of power losses from the inlet section because it contributes to increase solid temperatures at the absorber front section. However, such inlet power loss increase is only about 2% of the power regain. (Consequently, a negligible thermal efficiency decrease [ca. 0.13 pp] is registered for the case with the insulation layer in relation to the reference case with an adiabatic absorber lateral wall due to the contribution of the power regain on the power losses through the absorber front section.) The weak relevance of the power regain on the inlet power loss increase is due to two contrary behaviors developed while the solid (and fluid) temperatures increase at the absorber top-front region: (i) re-emission losses through the inlet section increase near the top-front region; and (ii) re-emission losses through the inlet section decrease near the centerline-front region because the flow distribution becomes more uniform along the radial direction and higher fluid velocities are observed at the receiver centerline (where the highest temperatures of the solid phase are observed) — note in Fig. 19 that solid temperatures near the centerline are lower for the highest power regain case than for the adiabatic lateral wall condition. However, the former effect is dominant and a slight increase in the inlet power loss is observed. It should be noted that for the cases with high lateral wall power losses the power regain (if non-negligible) may be unable to promote a significant temperature increase near the absorber front section. In such cases, the power loss through the inlet section decrease in relation to the adiabatic absorber lateral wall even though the total power loss increases due to the relevance of power losses through the insulation outer surface.

The previous investigation of the power regain effect on the thermal performance of volumetric solar receivers (with negligible receiver lateral wall power losses) shows that a more uniform temperature distribution at the receiver front section can be effectively achieved in relation to the adiabatic absorber lateral wall condition — see Fig. 19. Low solid temperature gradients are strongly beneficial to avoid high thermal stresses and ensure a long-term structural integrity of the absorber porous structure. The issue of non-uniform solid temperature distribution (hot-spots development) at the absorber front section — driven by an inhomogeneous solar flux distribution — has been addressed in the literature. Different strategies to obtain a more uniform absorber front temperature distribution have been proposed — see Section 1. As far as the authors are aware, the strategy related to the application of a high thermal conductivity material around the absorber porous structure to enhance the uniformity of the temperature distribution at the front section of volumetric solar absorbers was not previously reported.

#### 4.4. One-dimensional insulation model suitability

In this section, the receiver performance predicted applying the one-dimensional (1D) model for the insulation layer (1D heat conduction approximation along the radial direction) is compared with the receiver performance computed considering a multi-dimensional (MD) insulation model. The results are necessarily different because the temperature profile along the receiver longitudinal direction at the

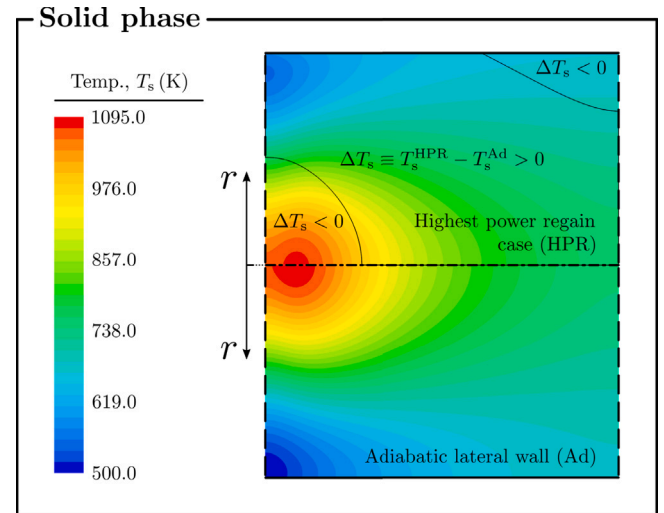


Fig. 19. Absorber solid-phase temperature distribution predicted for the insulation parameters and properties and external heat transfer conditions that lead to the highest power regain case (top) and for the adiabatic absorber lateral wall condition (bottom). The top inset shows the absorber regions of the highest power regain case that have a higher and lower solid-phase temperature than the adiabatic absorber lateral wall condition — regions where  $\Delta T_s > 0$  and  $\Delta T_s < 0$ , respectively.

absorber lateral wall ( $r = R_{\text{abs}}$ ) is not uniform. This implies that heat conduction in the insulation layer cannot be precisely 1D, even though a 1D heat conduction approximation — that requires a negligible computational cost — can be regarded as a suitable approximation. Figs. 20(a)–(c) present the difference between the receiver thermal efficiency predicted with the 1D insulation model and the receiver thermal efficiency predicted with the MD insulation model ( $\Delta \eta_{\text{th}} \equiv \eta_{\text{th}}^{\text{1D}} - \eta_{\text{th}}^{\text{MD}}$ ) for the same insulation parameters and properties and external conditions considered in Figs. 15(a)–(c).

For all insulation parameters and properties and external conditions considered, Figs. 20(a)–(c) show that the 1D model (slightly) overpredicts (or accurately predicts) the thermal efficiency — *i.e.*, the thermal efficiency computed with the 1D model is (slightly) higher than (or approximately equal to) the thermal efficiency computed applying the MD model. (Note that among the combinations considered the maximum difference is less than 0.4 pp.) The MD model computes higher (or similar) total power losses in comparison with the 1D model. For all combinations considered, inlet power losses predicted by the MD model are higher or approximately equal to those computed with the 1D model. This is due to the contribution of the power regain. (Note that the power regain cannot be accounted for through a 1D heat conduction approximation.) In Fig. 20(a), the differences observed for the cases with a negligible external overall heat transfer coefficient ( $h$  and  $\epsilon_{\text{w,ext}}$  equal to 0) are solely due to the effect of the power regain. For such cases, note that for a particular insulation thickness the difference increases as the thermal conductivity increases which is in full agreement with the power regain increasing relevance with the insulation thermal conductivity, as concluded in Section 4.3. Additionally, note that the 1D insulation model results for a negligible external overall heat transfer coefficient are independent of the insulation thickness and are equal to the results computed with an adiabatic absorber lateral wall. For a particular combination of insulation thickness and external heat transfer conditions, the thermal efficiency difference between both models decreases as the insulation thermal conductivity decreases. For the lowest insulation thermal conductivity value combined with non-negligible lateral wall power losses ( $U_{\text{ext}} \neq 0$ ), the differences between both modeling approaches are negligible for the considered insulation thickness range. For a specific insulation thermal conductivity, the thermal efficiency difference becomes independent of the external heat

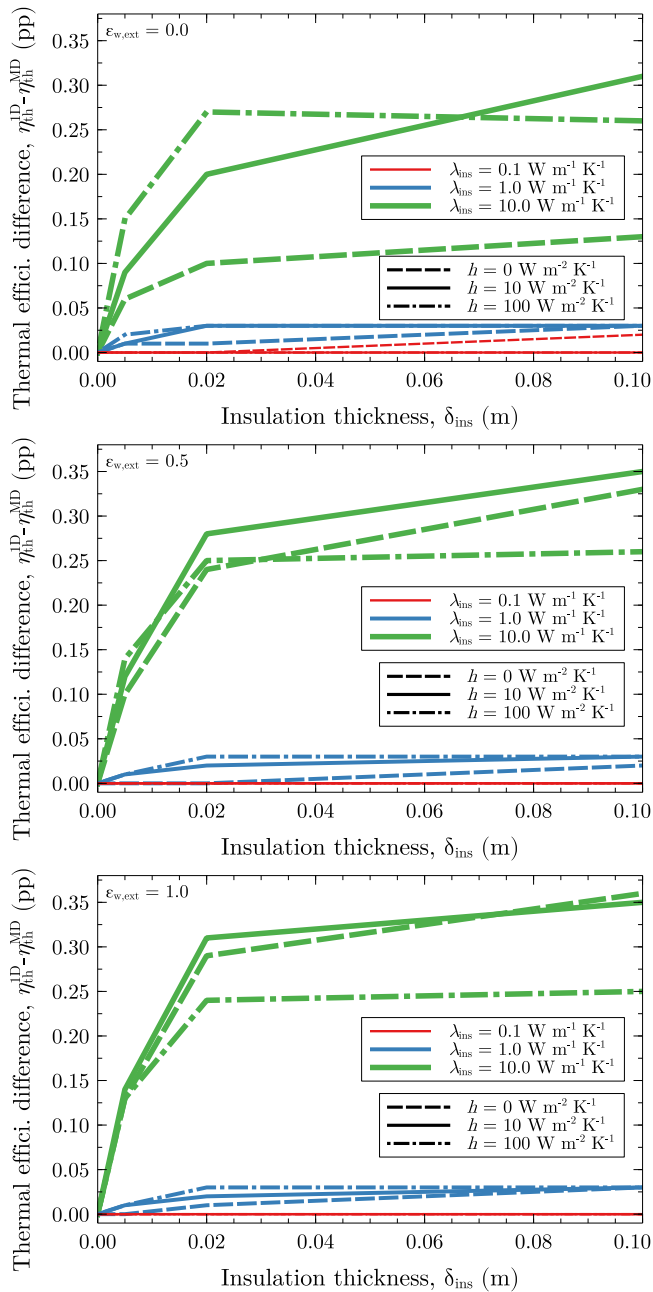


Fig. 20. Effect of the insulation thickness, insulation thermal conductivity, and external convection heat transfer coefficient on the difference between the receiver thermal efficiencies computed with the one-dimensional and multi-dimensional insulation models for three lateral wall external surface emissivity values: (a) 0.0; (b) 0.5; and (c) 1.0.

transfer conditions as the insulation thickness is increased. This is particularly noticeable in Figs. 20(a)–(c) for the intermediate insulation thermal conductivity value.

Fig. 21 presents the absorber solid- and gas-phase temperature distributions computed with the 1D and MD insulation models for an insulation thermal conductivity, insulation thickness, external surface emissivity, and convection heat transfer coefficient equal to  $10 \text{ W m}^{-1} \text{ K}^{-1}$ ,  $0.02 \text{ m}$ ,  $1.0$ , and  $10 \text{ W m}^{-2} \text{ K}^{-1}$ , respectively. This set of values corresponds to one of the poorest combinations for the suitability of the 1D insulation model — this case has a thermal efficiency difference of about 0.31 pp (see Fig. 20(c)). In Fig. 21, the temperature distribution for the insulation region is also presented for the MD modeling approach. Fig. 21 shows that both modeling strategies predict

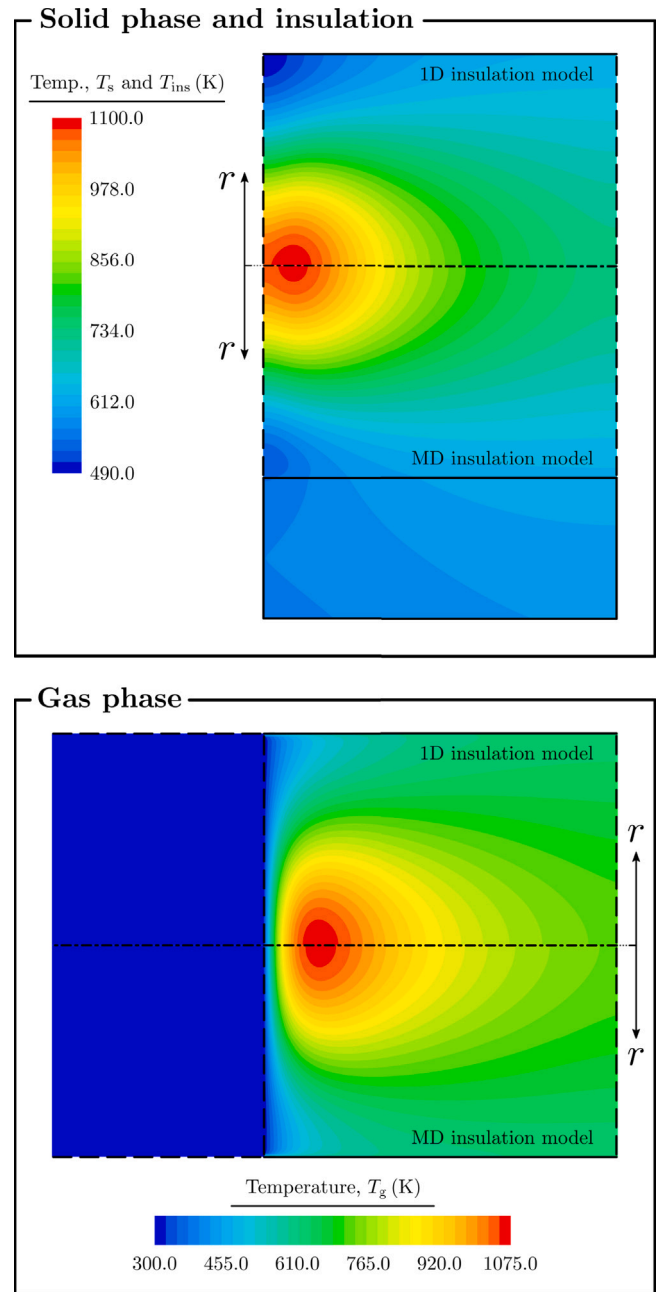


Fig. 21. Temperature distribution for the absorber solid phase and insulation material (top) and absorber gas phase (bottom) computed with the 1D and MD insulation models for an insulation thermal conductivity, insulation thickness, external surface emissivity, and convection heat transfer coefficient equal to  $10 \text{ W m}^{-1} \text{ K}^{-1}$ ,  $0.02 \text{ m}$ ,  $1.0$ , and  $10 \text{ W m}^{-2} \text{ K}^{-1}$ , respectively.

a comparable absorber thermal performance despite the case under consideration is one of the worst cases concerning the accuracy of the 1D insulation model for the thermal efficiency prediction. For this case, the difference between the (surface) average outlet temperatures between both models is only about 1.1 K. These results show that the 1D insulation model provides reasonable thermal performance predictions for volumetric solar receivers with lateral wall heat losses.

## 5. Conclusions

The non-ideal volumetric solar absorber operation is generally ascribed to power losses observed exclusively from the receiver inlet and outlet sections. Power losses from the absorber lateral wall have been commonly neglected in the literature — with benefits related to a simplified model formulation. In this work, the relevance of lateral wall heat losses on the operation of volumetric solar absorbers is comprehensively investigated. Volume-averaging and local thermal non-equilibrium models are considered with radiative heat transport taken into account through the modified P1 approximation. For the insulation layer applied at the absorber lateral surface, a multi-dimensional and one-dimensional heat diffusion models with consistent boundary and interface conditions are considered. Common values for parameters, properties, and conditions available in the literature are considered to conduct this study. The following conclusions can be drawn:

- An absorber with lateral wall heat losses presents higher temperatures at the absorber centerline and lower temperatures at the lateral wall than an absorber with an adiabatic lateral wall — this is observed because lateral wall heat losses promote a temperature decrease near the wall which leads the flow (whose properties are temperature-dependent) to preferentially deviated from the centerline region to the near wall region; consequently, more uneven temperature distributions (and higher solid-phase thermal gradients) are observed when lateral wall heat losses are registered which can promote an earlier absorber structural failure.
- Heat conduction from the absorber solid phase to the absorber lateral wall is the most relevant heat transfer route from the absorber internal region to the absorber lateral wall when lateral wall heat losses are considered; therefore, decreasing the effective solid thermal conductivity — achieved by increasing the absorber porosity or decreasing the intrinsic solid-phase thermal conductivity — results in lower power losses to the lateral wall (higher thermal efficiency).
- As the inlet velocity increases lateral wall heat losses decrease and the corresponding thermal efficiency approaches the thermal efficiency for the adiabatic absorber lateral wall condition.
- As the incident concentrated solar flux becomes more non-uniform for a constant maximum value (observed at the centerline) heat losses through the inlet section, and particularly, through the lateral wall decrease since lower solar flux values are provided to the receiver particularly near the lateral wall; as the incident concentrated solar flux becomes more non-uniform for a constant total solar power provided to receiver, lower solar flux values are observed near the wall and higher near the centerline, and consequently, lateral wall heat losses decrease and inlet power losses increase — for low maximum solar flux values this tradeoff leads to an increase in the thermal efficiency.
- Radiative heat transfer from the receiver lateral (external) surface has a limited effect on lateral wall power losses; the actual value for the external surface emissivity becomes less relevant on the receiver thermal efficiency as the convection heat transfer coefficients increases; the maximum thermal efficiency decrease from the adiabatic value (83.3%) due to radiative heat transfer is about 4.3 percentage points (observed for negligible convective heat losses in the absence of any insulation).
- Neglecting the application of an insulation layer and assuming a black lateral wall external surface, a decrease of about 5.6 percentage points on the thermal efficiency in relation to the adiabatic absorber lateral wall condition is estimated under natural convection conditions; moreover, this value increases significantly in the forced convection regime.
- The application of an insulation layer at the absorber lateral wall made of an unsuitable material for a particular set of external heat transfer conditions results in an actual promotion of heat losses and a decrease of thermal efficiency.
- The application of an insulation layer, particularly of a high thermal conductivity material, with a high insulation thickness and in an environment with a low external overall heat transfer coefficient promotes heat transport from downstream absorber regions to upstream absorber regions through the insulation material; advantage can be taken from this mechanism to uniformize (homogenize) the solid-phase temperature distribution, particularly near the absorber front section, to avoid excessive material thermal stresses; this conclusion suggests a novel design for a composite two-layer absorber lateral wall with a high thermal conductivity material in the inner layer and a low thermal conductivity material in the outer layer.
- A one-dimensional model for heat conduction in the insulation layer (receiver lateral wall) provides reasonable results for the thermal performance of volumetric solar absorbers — this conclusion is particularly important from the computational cost standpoint for future works aiming to account for lateral wall power losses.

### CRedit authorship contribution statement

**Jorge E.P. Navalho:** Writing – review & editing, Writing – original draft, Visualization, Validation, Software, Project administration, Methodology, Investigation, Conceptualization. **Laura G.G. Silva:** Writing – review & editing, Writing – original draft, Validation, Software, Investigation. **José C.F. Pereira:** Writing – review & editing, Resources.

### Declaration of competing interest

The authors declare that they have no known competing financial interests or personal relationships that could have appeared to influence the work reported in this paper.

### Data availability

Data will be made available on request.

### Acknowledgments

Authors acknowledge Fundação para a Ciência e a Tecnologia (FCT, I.P.), Portugal for its financial support via the projects UIDB/00667/2020 (UNIDEMI) and UIDP/00667/2020 (UNIDEMI).

### References

- [1] K. Ravi Kumar, N. Krishna Chaitanya, N. Sendhil Kumar, Solar thermal energy technologies and its applications for process heating and power generation – A review, *J. Clean. Prod.* 282 (2021) 125296, <http://dx.doi.org/10.1016/j.jclepro.2020.125296>, URL <https://www.sciencedirect.com/science/article/pii/S0959652620353415>.
- [2] G. Li, M. Li, R. Taylor, Y. Hao, G. Besagni, C. Markides, Solar energy utilisation: Current status and roll-out potential, *Appl. Therm. Eng.* 209 (2022) 118285, <http://dx.doi.org/10.1016/j.applthermaleng.2022.118285>, URL <https://www.sciencedirect.com/science/article/pii/S1359431122002447>.
- [3] W. Lipiński, E. Abbasi-Shavazi, J. Chen, J. Coventry, M. Hangi, S. Iyer, A. Kumar, L. Li, S. Li, J. Pye, J.F. Torres, B. Wang, Y. Wang, V.M. Wheeler, Progress in heat transfer research for high-temperature solar thermal applications, *Appl. Therm. Eng.* 184 (2021) 116137, <http://dx.doi.org/10.1016/j.applthermaleng.2020.116137>, URL <https://www.sciencedirect.com/science/article/pii/S1359431120336176>.
- [4] B. Wang, L. Li, F. Schäfer, J.J. Pottas, A. Kumar, V.M. Wheeler, W. Lipiński, Thermal reduction of iron-manganese oxide particles in a high-temperature packed-bed solar thermochemical reactor, *Chem. Eng. J.* 412 (2021) 128255, <http://dx.doi.org/10.1016/j.cej.2020.128255>, URL <https://www.sciencedirect.com/science/article/pii/S1385894720343680>.

- [5] J.E.P. Navalho, J.M.C. Pereira, A.R. Ervilha, J.C.F. Pereira, Uncertainty quantification in the catalytic partial oxidation of methane, *Combust. Theory Model.* 17 (6) (2013) 1067–1095, <http://dx.doi.org/10.1080/13647830.2013.826823>, arXiv:<https://doi.org/10.1080/13647830.2013.826823>.
- [6] J.E.P. Navalho, J.M.C. Pereira, J.C.F. Pereira, Conical-shaped foam reactors for catalytic partial oxidation applications, *Int. J. Hydrog. Energy* 39 (8) (2014) 3666–3680, <http://dx.doi.org/10.1016/j.ijhydene.2013.12.107>, URL <https://www.sciencedirect.com/science/article/pii/S0360319913030711>.
- [7] J.E.P. Navalho, J.M.C. Pereira, J.C.F. Pereira, Multiscale modeling of methane catalytic partial oxidation: From the mesopore to the full-scale reactor operation, *AIChE J.* 64 (2) (2018) 578–594, <http://dx.doi.org/10.1002/aic.15945>, arXiv:<https://aiche.onlinelibrary.wiley.com/doi/pdf/10.1002/aic.15945>, URL <https://aiche.onlinelibrary.wiley.com/doi/abs/10.1002/aic.15945>.
- [8] J.M.C. Pereira, J.E.P. Navalho, A.C.G. Amador, J.C.F. Pereira, Multi-scale modeling of diffusion and reaction-diffusion phenomena in catalytic porous layers: Comparison with the 1D approach, *Chem. Eng. Sci.* 117 (2014) 364–375, <http://dx.doi.org/10.1016/j.ces.2014.06.028>, URL <https://www.sciencedirect.com/science/article/pii/S0009250914003157>.
- [9] Y.-L. He, S. Du, S. Shen, Advances in porous volumetric solar receivers and enhancement of volumetric absorption, *Energy Rev.* 2 (3) (2023) 100035, <http://dx.doi.org/10.1016/j.enrev.2023.100035>, URL <https://www.sciencedirect.com/science/article/pii/S2772970223000226>.
- [10] M. Cagnoli, L. Savoldi, R. Zanino, F. Zaversky, Coupled optical and CFD parametric analysis of an open volumetric air receiver of honeycomb type for central tower CSP plants, *Sol. Energy* 155 (2017) 523–536, <http://dx.doi.org/10.1016/j.solener.2017.06.038>, URL <https://www.sciencedirect.com/science/article/pii/S0038092X17305479>.
- [11] J.E.P. Navalho, J.C.F. Pereira, A comprehensive and fully predictive discrete methodology for volumetric solar receivers: application to a functional parabolic dish solar collector system, *Appl. Energy* 267 (2020) 114781, <http://dx.doi.org/10.1016/j.apenergy.2020.114781>, URL <https://www.sciencedirect.com/science/article/pii/S0306261920302932>.
- [12] A.L. Avila-Marin, C. Caliot, M. Alvarez de Lara, J. Fernandez-Reche, M.J. Montes, A. Martinez-Tarifa, Homogeneous equivalent model coupled with P1-approximation for dense wire meshes volumetric air receivers, *Renew. Energy* 135 (2019) 908–919, <http://dx.doi.org/10.1016/j.renene.2018.12.061>, URL <https://www.sciencedirect.com/science/article/pii/S0960148118315052>.
- [13] A.L. Avila-Marin, CFD parametric analysis of wire meshes open volumetric receivers with axial-varied porosity and comparison with small-scale solar receiver tests, *Renew. Energy* 193 (2022) 1094–1105, <http://dx.doi.org/10.1016/j.renene.2022.05.060>, URL <https://www.sciencedirect.com/science/article/pii/S0960148122007017>.
- [14] Q. Zhu, Y. Xuan, Pore scale numerical simulation of heat transfer and flow in porous volumetric solar receivers, *Appl. Therm. Eng.* 120 (2017) 150–159, <http://dx.doi.org/10.1016/j.applthermaleng.2017.03.141>, URL <https://www.sciencedirect.com/science/article/pii/S1359431116324590>.
- [15] C. Pabst, G. Feckler, S. Schmitz, O. Smirnova, R. Capuano, P. Hirth, T. Fend, Experimental performance of an advanced metal volumetric air receiver for solar towers, *Renew. Energy* 106 (2017) 91–98, <http://dx.doi.org/10.1016/j.renene.2017.01.016>, URL <https://www.sciencedirect.com/science/article/pii/S0960148117300162>.
- [16] R. Capuano, T. Fend, H. Stadler, B. Hoffschmidt, R. Pitz-Paal, Optimized volumetric solar receiver: Thermal performance prediction and experimental validation, *Renew. Energy* 114 (2017) 556–566, <http://dx.doi.org/10.1016/j.renene.2017.07.071>, URL <https://www.sciencedirect.com/science/article/pii/S0960148117306997>.
- [17] S. Luque, G. Menéndez, M. Roccabruna, J. González-Aguilar, L. Crema, M. Romero, Exploiting volumetric effects in novel additively manufactured open solar receivers, *Sol. Energy* 174 (2018) 342–351, <http://dx.doi.org/10.1016/j.solener.2018.09.030>, URL <https://www.sciencedirect.com/science/article/pii/S0038092X18309022>.
- [18] X. Rández, F. Zaversky, D. Astrain, A novel active volumetric rotating disks solar receiver for concentrated solar power generation, *Appl. Therm. Eng.* 206 (2022) 118114, <http://dx.doi.org/10.1016/j.applthermaleng.2022.118114>, URL <https://www.sciencedirect.com/science/article/pii/S1359431122000783>.
- [19] J.M. Chavez, C. Chaza, Testing of a porous ceramic absorber for a volumetric air receiver, *Sol. Energy Mater.* 24 (1) (1991) 172–181, [http://dx.doi.org/10.1016/0165-1633\(91\)90057-R](http://dx.doi.org/10.1016/0165-1633(91)90057-R), URL <https://www.sciencedirect.com/science/article/pii/016516339190057R>.
- [20] A.L. Avila-Marin, Volumetric receivers in solar thermal power plants with central receiver system technology: A review, *Sol. Energy* 85 (5) (2011) 891–910, <http://dx.doi.org/10.1016/j.solener.2011.02.002>, URL <https://www.sciencedirect.com/science/article/pii/S0038092X11000302>.
- [21] S. Mey-Cloutier, C. Caliot, A. Kribus, Y. Gray, G. Flamant, Experimental study of ceramic foams used as high temperature volumetric solar absorber, *Sol. Energy* 136 (2016) 226–235, <http://dx.doi.org/10.1016/j.solener.2016.06.066>, URL <https://www.sciencedirect.com/science/article/pii/S0038092X1630247X>.
- [22] A. Avila-Marin, J. Fernandez-Reche, A. Martinez-Tarifa, Modelling strategies for porous structures as solar receivers in central receiver systems: A review, *Renew. Sustain. Energy Rev.* 111 (2019) 15–33, <http://dx.doi.org/10.1016/j.rser.2019.03.059>, URL <https://www.sciencedirect.com/science/article/pii/S1364032119301996>.
- [23] A. Godini, S. Kheradmand, Optimization of volumetric solar receiver geometry and porous media specifications, *Renew. Energy* 172 (2021) 574–581, <http://dx.doi.org/10.1016/j.renene.2021.03.040>, URL <https://www.sciencedirect.com/science/article/pii/S0960148121003943>.
- [24] B. Guene Lougou, Y. Shuai, R. Pan, G. Chaffa, H. Tan, Heat transfer and fluid flow analysis of porous medium solar thermochemical reactor with quartz glass cover, *Int. J. Heat Mass Transfer* 127 (2018) 61–74, <http://dx.doi.org/10.1016/j.ijheatmasstransfer.2018.06.153>, URL <https://www.sciencedirect.com/science/article/pii/S0017931018306525>.
- [25] H. Zhang, Y. Shuai, Y. Yuan, B. Guene Lougou, B. Jiang, F. Wang, Z. Cheng, Thermal-chemical reaction characteristics of Ni/Al<sub>2</sub>O<sub>3</sub> catalytic porous material filled solar reactor for dry reforming of methane process, *Appl. Therm. Eng.* 180 (2020) 115901, <http://dx.doi.org/10.1016/j.applthermaleng.2020.115901>, URL <https://www.sciencedirect.com/science/article/pii/S1359431120333834>.
- [26] Z. Wu, C. Caliot, G. Flamant, Z. Wang, Coupled radiation and flow modeling in ceramic foam volumetric solar air receivers, *Sol. Energy* 85 (9) (2011) 2374–2385, <http://dx.doi.org/10.1016/j.solener.2011.06.030>, URL <https://www.sciencedirect.com/science/article/pii/S0038092X11002428>.
- [27] A. Kribus, Y. Gray, M. Grijnevich, G. Mittelman, S. Mey-Cloutier, C. Caliot, The promise and challenge of solar volumetric absorbers, *Sol. Energy* 110 (2014) 463–481, <http://dx.doi.org/10.1016/j.solener.2014.09.035>, URL <https://www.sciencedirect.com/science/article/pii/S0038092X14004757>.
- [28] X. Chen, X.-L. Xia, X.-W. Yan, C. Sun, Heat transfer analysis of a volumetric solar receiver with composite porous structure, *Energy Convers. Manage.* 136 (2017) 262–269, <http://dx.doi.org/10.1016/j.enconman.2017.01.018>, URL <https://www.sciencedirect.com/science/article/pii/S0196890417300183>.
- [29] X. Chen, X.-L. Xia, H. Liu, Y. Li, B. Liu, Heat transfer analysis of a volumetric solar receiver by coupling the solar radiation transport and internal heat transfer, *Energy Convers. Manage.* 114 (2016) 20–27, <http://dx.doi.org/10.1016/j.enconman.2016.01.074>, URL <https://www.sciencedirect.com/science/article/pii/S019689041630022X>.
- [30] G. Barreto, P. Canhoto, M. Collares-Pereira, Three-dimensional CFD modelling and thermal performance analysis of porous volumetric receivers coupled to solar concentration systems, *Appl. Energy* 252 (2019) 113433, <http://dx.doi.org/10.1016/j.apenergy.2019.113433>, URL <https://www.sciencedirect.com/science/article/pii/S0306261919311079>.
- [31] X.-Y. Tang, K.-R. Zhang, W.-W. Yang, P.-Y. Dou, Integrated design of solar concentrator and thermochemical reactor guided by optimal solar radiation distribution, *Energy* 263 (2023) 125828, <http://dx.doi.org/10.1016/j.energy.2022.125828>, URL <https://www.sciencedirect.com/science/article/pii/S0360544222027141>.
- [32] F. Zaversky, L. Aldaz, M. Sánchez, A.L. Avila-Marin, M.I. Roldán, J. Fernández-Reche, A. Füssel, W. Beckert, J. Adler, Numerical and experimental evaluation and optimization of ceramic foam as solar absorber – Single-layer vs multi-layer configurations, *Appl. Energy* 210 (2018) 351–375, <http://dx.doi.org/10.1016/j.apenergy.2017.11.003>, URL <https://www.sciencedirect.com/science/article/pii/S0306261917315787>.
- [33] W. Liu, G. Wei, P. Huang, C. Xu, X. Du, Design and performance analysis of volumetric solar receiver based on porous foam ceramics, *AIP Conf. Proc.* 2033 (1) (2018) 040022, <http://dx.doi.org/10.1063/1.5067058>, arXiv:[https://pubs.aip.org/aip/acp/article-pdf/doi/10.1063/1.5067058/13993773/040022\\_1\\_online.pdf](https://pubs.aip.org/aip/acp/article-pdf/doi/10.1063/1.5067058/13993773/040022_1_online.pdf).
- [34] S. Du, Z. Li, Y. He, D. Li, X. Xie, Y. Gao, Experimental and numerical analysis of the hydraulic and thermal performances of the gradually-varied porous volumetric solar receiver, *Sci. China Technol. Sci.* 63 (7) (2020) 1224–1234, <http://dx.doi.org/10.1007/s11431-020-1580-2>.
- [35] F. Wang, J. Tan, Y. Shuai, L. Gong, H. Tan, Numerical analysis of hydrogen production via methane steam reforming in porous media solar thermochemical reactor using concentrated solar irradiation as heat source, *Energy Convers. Manage.* 87 (2014) 956–964, <http://dx.doi.org/10.1016/j.enconman.2014.08.003>, URL <https://www.sciencedirect.com/science/article/pii/S0196890414007274>.
- [36] F. Wang, J. Tan, L. Ma, Y. Leng, Effects of key factors on solar aided methane steam reforming in porous medium thermochemical reactor, *Energy Convers. Manage.* 103 (2015) 419–430, <http://dx.doi.org/10.1016/j.enconman.2015.06.049>, URL <https://www.sciencedirect.com/science/article/pii/S0196890415005907>.
- [37] A. Kribus, M. Grijnevich, Y. Gray, C. Caliot, Parametric study of volumetric absorber performance, *Energy Procedia* 49 (2014) 408–417, <http://dx.doi.org/10.1016/j.egypro.2014.03.044>, URL <https://www.sciencedirect.com/science/article/pii/S1876610214004986>, Proceedings of the SolarPACES 2013 International Conference.
- [38] F. Wang, J. Tan, Z. Wang, Heat transfer analysis of porous media receiver with different transport and thermophysical models using mixture as feeding gas, *Energy Convers. Manage.* 83 (2014) 159–166, <http://dx.doi.org/10.1016/j.enconman.2014.03.068>, URL <https://www.sciencedirect.com/science/article/pii/S0196890414002696>.

- [39] A. Andreozzi, N. Bianco, M. Iasiello, V. Naso, Thermo-fluid-dynamics of a ceramic foam solar receiver: A parametric analysis, *Heat Transf. Eng.* 41 (12) (2020) 1085–1099, <http://dx.doi.org/10.1080/01457632.2019.1600876>, arXiv: <https://doi.org/10.1080/01457632.2019.1600876>.
- [40] M. Roldán, O. Smirnova, T. Fend, J. Casas, E. Zarza, Thermal analysis and design of a volumetric solar absorber depending on the porosity, *Renew. Energy* 62 (2014) 116–128, <http://dx.doi.org/10.1016/j.renene.2013.06.043>, URL <https://www.sciencedirect.com/science/article/pii/S0960148113003364>.
- [41] A. Andreozzi, N. Bianco, M. Iasiello, V. Naso, Thermal analysis of an open cell foam volumetric solar receiver, *Int. J. Heat Technol.* 34 (2) (2016) S489–S495, <http://dx.doi.org/10.18280/ijht.34S242>, URL <https://www.sciencedirect.com/science/article/pii/016516339190057R>.
- [42] H. Zhang, B. Guene Lougou, R. Pan, Y. Shuai, F. Wang, Z. Cheng, H. Tan, Analysis of thermal transport and fluid flow in high-temperature porous media solar thermochemical reactor, *Sol. Energy* 173 (2018) 814–824, <http://dx.doi.org/10.1016/j.solener.2018.08.015>, URL <https://www.sciencedirect.com/science/article/pii/S0038092X18307849>.
- [43] J.E.P. Navalho, J.C.F. Pereira, Investigating the impact of modeling assumptions and closure models on the steady-state prediction of solar-driven methane steam reforming in a porous reactor, *Energy Convers. Manage.* 295 (2023) 117577, <http://dx.doi.org/10.1016/j.enconman.2023.117577>, URL <https://www.sciencedirect.com/science/article/pii/S0196890423009238>.
- [44] C. Xu, Z. Song, L. der Chen, Y. Zhen, Numerical investigation on porous media heat transfer in a solar tower receiver, *Renew. Energy* 36 (3) (2011) 1138–1144, <http://dx.doi.org/10.1016/j.renene.2010.09.017>, URL <https://www.sciencedirect.com/science/article/pii/S0960148110004489>.
- [45] F. Wang, Y. Shuai, Z. Wang, Y. Leng, H. Tan, Thermal and chemical reaction performance analyses of steam methane reforming in porous media solar thermochemical reactor, *Int. J. Hydrog. Energy* 39 (2) (2014) 718–730, <http://dx.doi.org/10.1016/j.ijhydene.2013.10.132>, URL <https://www.sciencedirect.com/science/article/pii/S0360319913026475>.
- [46] X. Ni, T. Liu, D. Liu, Effects of volumetric property models on the efficiency of a porous volumetric solar receiver, *Energies* 15 (11) (2022) <http://dx.doi.org/10.3390/en15113899>, URL <https://www.mdpi.com/1996-1073/15/11/3899>.
- [47] F. Wang, J. Tan, S. Yong, H. Tan, S. Chu, Thermal performance analyses of porous media solar receiver with different irradiative transfer models, *Int. J. Heat Mass Transfer* 78 (2014) 7–16, <http://dx.doi.org/10.1016/j.ijheatmasstransfer.2014.06.035>, URL <https://www.sciencedirect.com/science/article/pii/S0017931014005079>.
- [48] S. Mey, C. Caliot, G. Flamant, A. Kribus, Y. Gray, Optimization of high temperature SiC volumetric solar absorber, *Energy Procedia* 49 (2014) 478–487, <http://dx.doi.org/10.1016/j.egypro.2014.03.051>, URL <https://www.sciencedirect.com/science/article/pii/S1876610214005050>, Proceedings of the SolarPACES 2013 International Conference.
- [49] X. Chen, F. Wang, X. Yan, Z. Cheng, Y. Han, Z. Jie, Thermal and chemical analysis of methane dry reforming in a volumetric reactor under highly concentrated solar radiation, *Sol. Energy* 162 (2018) 187–195, <http://dx.doi.org/10.1016/j.solener.2018.01.032>, URL <https://www.sciencedirect.com/science/article/pii/S0038092X18300537>.
- [50] P. Wang, K. Vafai, D. Liu, C. Xu, Analysis of collimated irradiation under local thermal non-equilibrium condition in a packed bed, *Int. J. Heat Mass Transfer* 80 (2015) 789–801, <http://dx.doi.org/10.1016/j.ijheatmasstransfer.2014.09.021>, URL <https://www.sciencedirect.com/science/article/pii/S0017931014008138>.
- [51] C. Caliot, P.-M. Déjardin, Numerical demonstration of the volumetric effect in a high specific surface absorber with Kelvin cells, *AIP Conf. Proc.* 2126 (1) (2019) 030011, <http://dx.doi.org/10.1063/1.5117523>, arXiv: [https://pubs.aip.org/aip/acp/article-pdf/doi/10.1063/1.5117523/14189249/030011\\_1\\_online.pdf](https://pubs.aip.org/aip/acp/article-pdf/doi/10.1063/1.5117523/14189249/030011_1_online.pdf).
- [52] X. Chen, J. Lyu, C. Sun, X. Xia, F. Wang, Pore-scale evaluation on a volumetric solar receiver with different optical property control strategies, *Energy* 278 (2023) 128006, <http://dx.doi.org/10.1016/j.energy.2023.128006>, URL <https://www.sciencedirect.com/science/article/pii/S0360544223014007>.
- [53] S. Du, M.-J. Li, Q. Ren, Q. Liang, Y.-L. He, Pore-scale numerical simulation of fully coupled heat transfer process in porous volumetric solar receiver, *Energy* 140 (2017) 1267–1275, <http://dx.doi.org/10.1016/j.energy.2017.08.062>, URL <https://www.sciencedirect.com/science/article/pii/S0360544217314408>.
- [54] S. Du, M.-J. Li, Y.-L. He, S. Shen, Conceptual design of porous volumetric solar receiver using molten salt as heat transfer fluid, *Appl. Energy* 301 (2021) 117400, <http://dx.doi.org/10.1016/j.apenergy.2021.117400>, URL <https://www.sciencedirect.com/science/article/pii/S0360544221008011>.
- [55] M. Faizan, A. Almerbati, B. Yilbas, A novel approach for volumetric solar receiver performance assessments, *Appl. Therm. Eng.* 211 (2022) 118487, <http://dx.doi.org/10.1016/j.applthermaleng.2022.118487>, URL <https://www.sciencedirect.com/science/article/pii/S1359431122004410>.
- [56] Z. Wu, C. Caliot, G. Flamant, Z. Wang, Numerical simulation of convective heat transfer between air flow and ceramic foams to optimise volumetric solar air receiver performances, *Int. J. Heat Mass Transfer* 54 (7) (2011) 1527–1537, <http://dx.doi.org/10.1016/j.ijheatmasstransfer.2010.11.037>, URL <https://www.sciencedirect.com/science/article/pii/S0017931010006514>.
- [57] S. Du, Z.-X. Tong, H.-H. Zhang, Y.-L. He, Tomography-based determination of nusselt number correlation for the porous volumetric solar receiver with different geometrical parameters, *Renew. Energy* 135 (2019) 711–718, <http://dx.doi.org/10.1016/j.renene.2018.12.001>, URL <https://www.sciencedirect.com/science/article/pii/S0960148118314320>.
- [58] X.-L. Li, C. Sun, X.-L. Xia, Z.-H. Li, Y. Li, Modeling of coupled heat transfer in a windowed volumetric solar receiver, *Sol. Energy* 201 (2020) 195–208, <http://dx.doi.org/10.1016/j.solener.2020.02.073>, URL <https://www.sciencedirect.com/science/article/pii/S0038092X20302000>.
- [59] X. Chen, X.-L. Xia, X.-L. Meng, X.-H. Dong, Thermal performance analysis on a volumetric solar receiver with double-layer ceramic foam, *Energy Convers. Manage.* 97 (2015) 282–289, <http://dx.doi.org/10.1016/j.enconman.2015.03.066>, URL <https://www.sciencedirect.com/science/article/pii/S0196890415002848>.
- [60] S. Du, T. Xia, Y.-L. He, Z.-Y. Li, D. Li, X.-Q. Xie, Experiment and optimization study on the radial graded porous volumetric solar receiver matching non-uniform solar flux distribution, *Appl. Energy* 275 (2020) 115343, <http://dx.doi.org/10.1016/j.apenergy.2020.115343>, URL <https://www.sciencedirect.com/science/article/pii/S0306261920308552>.
- [61] P. Wang, J. Li, F. Bai, D. Liu, C. Xu, L. Zhao, Z. Wang, Experimental and theoretical evaluation on the thermal performance of a windowed volumetric solar receiver, *Energy* 119 (2017) 652–661, <http://dx.doi.org/10.1016/j.energy.2016.11.024>, URL <https://www.sciencedirect.com/science/article/pii/S0360544216316309>.
- [62] K. Reddy, S. Nataraj, Thermal analysis of porous volumetric receivers of concentrated solar dish and tower systems, *Renew. Energy* 132 (2019) 786–797, <http://dx.doi.org/10.1016/j.renene.2018.08.030>, URL <https://www.sciencedirect.com/science/article/pii/S0960148118309807>.
- [63] F. Wang, Y. Shuai, H. Tan, C. Yu, Thermal performance analysis of porous media receiver with concentrated solar irradiation, *Int. J. Heat Mass Transfer* 62 (2013) 247–254, <http://dx.doi.org/10.1016/j.ijheatmasstransfer.2013.03.003>, URL <https://www.sciencedirect.com/science/article/pii/S0017931013002081>.
- [64] W. Fuqiang, T. Jianyu, J. Huijian, L. Yu, Thermochemical performance analysis of solar driven CO<sub>2</sub> methane reforming, *Energy* 91 (2015) 645–654, <http://dx.doi.org/10.1016/j.energy.2015.08.080>, URL <https://www.sciencedirect.com/science/article/pii/S0360544215011561>.
- [65] Y. Ren, H. Qi, J. Shi, Q. Chen, Y. Wang, L. Ruan, Thermal performance characteristics of porous media receiver exposed to concentrated solar radiation, *J. Energy Eng.* 143 (5) (2017) 04017013, [http://dx.doi.org/10.1061/\(ASCE\)EY.1943-7897.0000448](http://dx.doi.org/10.1061/(ASCE)EY.1943-7897.0000448), arXiv: <https://ascelibrary.org/doi/pdf/10.1061/%28ASCE%29EY.1943-7897.0000448>, URL <https://ascelibrary.org/doi/abs/10.1061/%28ASCE%29EY.1943-7897.0000448>.
- [66] Z. Wu, Z. Wang, Fully coupled transient modeling of ceramic foam volumetric solar air receiver, *Sol. Energy* 89 (2013) 122–133, <http://dx.doi.org/10.1016/j.solener.2012.12.016>, URL <https://www.sciencedirect.com/science/article/pii/S0038092X12004392>.
- [67] W. Fuqiang, G. Zhennan, T. Jianyu, M. Lanxin, Y. Zhenyu, T. Heping, Transient thermal performance response characteristics of porous-medium receiver heated by multi-dish concentrator, *Int. Commun. Heat Mass Transfer* 75 (2016) 36–41, <http://dx.doi.org/10.1016/j.icheatmasstransfer.2016.03.028>, URL <https://www.sciencedirect.com/science/article/pii/S0735193316300999>.
- [68] T. Fend, B. Hoffschmidt, R. Pitz-Paal, O. Reutter, P. Rietbrock, Porous materials as open volumetric solar receivers: Experimental determination of thermophysical and heat transfer properties, *Energy* 29 (5) (2004) 823–833, [http://dx.doi.org/10.1016/S0360-5442\(03\)00188-9](http://dx.doi.org/10.1016/S0360-5442(03)00188-9), URL <https://www.sciencedirect.com/science/article/pii/S0360544203001889>, SolarPACES 2002.
- [69] Y.-L. He, K. Wang, Y. Qiu, B.-C. Du, Q. Liang, S. Du, Review of the solar flux distribution in concentrated solar power: Non-uniform features, challenges, and solutions, *Appl. Therm. Eng.* 149 (2019) 448–474, <http://dx.doi.org/10.1016/j.applthermaleng.2018.12.006>, URL <https://www.sciencedirect.com/science/article/pii/S1359431118360769>.
- [70] M.E. Nimvari, N.F. Jouybari, Q. Esmaili, A new approach to mitigate intense temperature gradients in ceramic foam solar receivers, *Renew. Energy* 122 (2018) 206–215, <http://dx.doi.org/10.1016/j.renene.2018.01.117>, URL <https://www.sciencedirect.com/science/article/pii/S0960148118301277>.
- [71] X. Shi, F. Wang, B.G. Lougou, H. Zhang, X. Wei, D. Li, J. Xu, Experimental and numerical study regarding the biomimetic bone porous structure to match energy and mass flow in a solar thermochemical reactor, *J. Energy Storage* 55 (2022) 105645, <http://dx.doi.org/10.1016/j.est.2022.105645>, URL <https://www.sciencedirect.com/science/article/pii/S2352152X22016334>.
- [72] X.-L. Li, X.-L. Xia, C. Sun, Z.-H. Chen, Performance analysis on a volumetric solar receiver with an annular inner window, *Renew. Energy* 170 (2021) 487–499, <http://dx.doi.org/10.1016/j.renene.2021.01.141>, URL <https://www.sciencedirect.com/science/article/pii/S0960148121001543>.
- [73] H. Zhang, Y. Shuai, B.G. Lougou, B. Jiang, D. Yang, Q. Pan, F. Wang, X. Huang, Effects of foam structure on thermochemical characteristics of porous-filled solar reactor, *Energy* 239 (2022) 122219, <http://dx.doi.org/10.1016/j.energy.2021.122219>, URL <https://www.sciencedirect.com/science/article/pii/S0360544221024671>.

- [74] B. Guene Lougou, L. Wu, D. Ma, B. Geng, B. Jiang, D. Han, H. Zhang, P. Łapka, Y. Shuai, Efficient conversion of solar energy through a macroporous ceramic receiver coupling heat transfer and thermochemical reactions, *Energy* 271 (2023) 126989, <http://dx.doi.org/10.1016/j.energy.2023.126989>, URL <https://www.sciencedirect.com/science/article/pii/S0360544223003833>.
- [75] Y. Getahun Dessie, B. Guene Lougou, Q. Hong, T. Heping, Z. Juqi, G. Baohai, I. Md Arafat, Thermal performance analysis of a solar reactor designed for syngas production, *Energies* 13 (13) (2020) <http://dx.doi.org/10.3390/en13133405>, URL <https://www.mdpi.com/1996-1073/13/13/3405>.
- [76] T. Ma, M. Fu, J. Cong, X. Zhang, Q. Zhang, K.F. Sayfiyeva, Z. Chang, X. Li, Analysis of heat and mass transfer in a porous solar thermochemical reactor, *Energy* 294 (2024) 130842, <http://dx.doi.org/10.1016/j.energy.2024.130842>, URL <https://www.sciencedirect.com/science/article/pii/S0360544224006145>.
- [77] S. Bellan, T. Kodama, K. Matsubara, N. Gokon, H.S. Cho, K. Inoue, Heat transfer and particulate flow analysis of a 30 kW directly irradiated solar fluidized bed reactor for thermochemical cycling, *Chem. Eng. Sci.* 203 (2019) 511–525, <http://dx.doi.org/10.1016/j.ces.2018.09.012>, URL <https://www.sciencedirect.com/science/article/pii/S0009250918306596>.
- [78] B. Guene Lougou, D. Han, H. Zhang, B. Jiang, J. Anees, C. Ahouannou, J. Zhao, Y. Shuai, Numerical and experimental analysis of reactor optimum design and solar thermal-chemical energy conversion for multidisciplinary applications, *Energy Convers. Manage.* 213 (2020) 112870, <http://dx.doi.org/10.1016/j.enconman.2020.112870>, URL <https://www.sciencedirect.com/science/article/pii/S0196890420304088>.
- [79] Z. Wu, C. Caliot, F. Bai, G. Flamant, Z. Wang, J. Zhang, C. Tian, Experimental and numerical studies of the pressure drop in ceramic foams for volumetric solar receiver applications, *Appl. Energy* 87 (2) (2010) 504–513, <http://dx.doi.org/10.1016/j.apenergy.2009.08.009>, URL <https://www.sciencedirect.com/science/article/pii/S0360261909003122>.
- [80] S. Du, Y.-L. He, W.-W. Yang, Z.-B. Liu, Optimization method for the porous volumetric solar receiver coupling genetic algorithm and heat transfer analysis, *Int. J. Heat Mass Transfer* 122 (2018) 383–390, <http://dx.doi.org/10.1016/j.ijheatmasstransfer.2018.01.120>, URL <https://www.sciencedirect.com/science/article/pii/S0017931017347853>.
- [81] M. Schuetz, L. Glicksman, A basic study of heat transfer through foam insulation, *J. Cell. Plast.* 20 (2) (1984) 114–121.
- [82] R. Lemlich, A theory for the limiting conductivity of polyhedral foam at low density, *J. Colloid Interface Sci.* 64 (1) (1978) 107–110, [http://dx.doi.org/10.1016/0021-9797\(78\)90339-9](http://dx.doi.org/10.1016/0021-9797(78)90339-9), URL <http://www.sciencedirect.com/science/article/pii/0021979778903399>.
- [83] X. Chen, F. Wang, Y. Han, R. Yu, Z. Cheng, Thermochemical storage analysis of the dry reforming of methane in foam solar reactor, *Energy Convers. Manage.* 158 (2018) 489–498, <http://dx.doi.org/10.1016/j.enconman.2017.12.066>, URL <https://www.sciencedirect.com/science/article/pii/S0196890417312189>.
- [84] X. Shi, Y. Shuai, F. Wang, C. Zhang, Z. Cheng, X. Chen, Effects of ordered hierarchically porous structure on methane reforming performance in solar foam reactor, *J. CO<sub>2</sub> Util.* 37 (2020) 147–157, <http://dx.doi.org/10.1016/j.jcou.2019.12.002>, URL <https://www.sciencedirect.com/science/article/pii/S2212982019310844>.
- [85] H. Villafán-Vidales, S. Abanades, C. Caliot, H. Romero-Paredes, Heat transfer simulation in a thermochemical solar reactor based on a volumetric porous receiver, *Appl. Therm. Eng.* 31 (16) (2011) 3377–3386, <http://dx.doi.org/10.1016/j.applthermaleng.2011.06.022>, URL <https://www.sciencedirect.com/science/article/pii/S1359431111003322>.
- [86] W. Fuqiang, C. Ziming, T. Jianyu, Z. Jiaqi, L. Yu, L. Linhua, Energy storage efficiency analyses of CO<sub>2</sub> reforming of methane in metal foam solar thermochemical reactor, *Appl. Therm. Eng.* 111 (2017) 1091–1100, <http://dx.doi.org/10.1016/j.applthermaleng.2016.10.025>, URL <https://www.sciencedirect.com/science/article/pii/S1359431116322207>.
- [87] F.M. White, *Fluid Mechanics, Eighth Edition*, McGraw-Hill Education, 2016.
- [88] X. Chen, F. Wang, X. Yan, Y. Han, Z. Cheng, Z. Jie, Thermochemical performance of solar driven CO<sub>2</sub> reforming of methane in volumetric reactor with gradual foam structure, *Energy* 151 (2018) 545–555, <http://dx.doi.org/10.1016/j.energy.2018.03.086>, URL <https://www.sciencedirect.com/science/article/pii/S036054421830495X>.
- [89] X. Shi, F. Wang, Z. Cheng, H. Liang, Y. Dong, X. Chen, Numerical analysis of the biomimetic leaf-type hierarchical porous structure to improve the energy storage efficiency of solar driven steam methane reforming, *Int. J. Hydrog. Energy* 46 (34) (2021) 17653–17665, <http://dx.doi.org/10.1016/j.ijhydene.2021.02.171>, URL <https://www.sciencedirect.com/science/article/pii/S036031992100745X>, Special issue on the 2nd International Symposium on Hydrogen Energy and Energy Technologies (HEET 2019).
- [90] X. Shi, Y. Xun, Y. Dong, F. Wang, X. Zhang, Z. Cheng, Analysis of biomimetic hierarchical porous structure regulating radiation field to improve solar thermochemical performance based on minimum gibbs free energy, *Int. J. Hydrog. Energy* 47 (5) (2022) 2832–2845, <http://dx.doi.org/10.1016/j.ijhydene.2021.10.246>, URL <https://www.sciencedirect.com/science/article/pii/S0360319921043561>, Hydrogen Energy and Fuel Cells.
- [91] Y.-J. Yang, W.-W. Yang, X. Ma, X.-Y. Tang, X.E. Cao, Performance improvement of a solar volumetric reactor with passive thermal management under different solar radiation conditions, *Int. J. Hydrog. Energy* 48 (53) (2023) 20193–20207, <http://dx.doi.org/10.1016/j.ijhydene.2023.02.102>, URL <https://www.sciencedirect.com/science/article/pii/S0360319923009588>.
- [92] P.J. Roache, *Verification and Validation in Computational Science and Engineering*, Vol. 895, Hermosa Albuquerque, NM, 1998.
- [93] X. Chen, X. lin Xia, X. hong Dong, G. long Dai, Integrated analysis on the volumetric absorption characteristics and optical performance for a porous media receiver, *Energy Convers. Manage.* 105 (2015) 562–569, <http://dx.doi.org/10.1016/j.enconman.2015.08.028>, URL <https://www.sciencedirect.com/science/article/pii/S0196890415007748>.
- [94] F. Gomez-Garcia, S. Santiago, S. Luque, M. Romero, J. Gonzalez-Aguilar, A new laboratory-scale experimental facility for detailed aerothermal characterizations of volumetric absorbers, *AIP Conf. Proc.* 1734 (1) (2016) 030018, <http://dx.doi.org/10.1063/1.4949070>, arXiv:[https://pubs.aip.org/aip/acp/article-pdf/doi/10.1063/1.4949070/12828212/030018\\_1\\_online.pdf](https://pubs.aip.org/aip/acp/article-pdf/doi/10.1063/1.4949070/12828212/030018_1_online.pdf).
- [95] S.W. Churchill, H.H. Chu, Correlating equations for laminar and turbulent free convection from a horizontal cylinder, *Int. J. Heat Mass Transfer* 18 (9) (1975) 1049–1053, [http://dx.doi.org/10.1016/0017-9310\(75\)90222-7](http://dx.doi.org/10.1016/0017-9310(75)90222-7), URL <https://www.sciencedirect.com/science/article/pii/0017931075902227>.
- [96] S.W. Churchill, M. Bernstein, A correlating equation for forced convection from gases and liquids to a circular cylinder in crossflow, *J. Heat Transfer* 99 (2) (1977) 300–306, <http://dx.doi.org/10.1115/1.3450685>, arXiv:[https://asmdigitalcollection.asme.org/heattransfer/article-pdf/99/2/300/5909086/300\\_1.pdf](https://asmdigitalcollection.asme.org/heattransfer/article-pdf/99/2/300/5909086/300_1.pdf).
- [97] F.P. Incropera, D.P. DeWitt, T.L. Bergman, A.S. Lavine, *Fundamentals of Heat and Mass Transfer*, Sixth ed., John Wiley & Sons, 2007.